國立交通大學

電子物理研究所

博 士 論 文

高品質氧化鋅、氧化鎂鋅、氧化錳鋅與氧化鎘鋅之成長與光學研究

Growth and optical study of high quality ZnO, ZnMgO, ZnMnO and ZnCdO

研 究 生：簡崑峯

指導教授：周武清　教授

中 華 民 國 一 百 零 二 年 七 月

高品質氧化鋅、氧化鎂鋅、氧化錳鋅與氧化鎘鋅之成長與光學研究

Growth and Optical Study of High Quality ZnO, ZnMgO, ZnMnO and ZnCdO

研 究 生：簡崑峯　　Student：Kun-Feng Chien

指導教授： 周武清 教授　　Advisor：Prof. Wu-Ching Chou

國 立 交 通 大 學

電 子 物 理 研 究 所

博 士 論 文

A Dissertation

Submitted to Institute of Electrophysics

College of Science

National Chiao Tung University

in Partial Fulfillment of the Requirements

for the Degree of

Doctor of Philosophy

in

Electrophysics

July 2013

Hsinchu, Taiwan, Republic of China

中華民國一百零二年七月

高品質氧化鋅、氧化鎂鋅、氧化錳鋅與氧化鎘鋅之成長與光學研究

研究生：簡崑峯　　指導教授：周武清 教授

國立交通大學電子物理研究所

中文摘要

本篇論文利用電漿輔助式分子束磊晶系統在藍寶石基板上成長高品質氧化鋅、氧化鎂鋅、氧化錳鋅與氧化鎘鋅薄膜，並利用光頻譜量測技術探討樣品的光學特性。

在氧化鋅部分，利用固定氧氣流量，調控鋅元素流量，成長出不同參數之氧化鋅薄膜。經由光激螢光光譜量測，得到一組氧化鋅薄膜發光最佳品質之樣品。接續的氧化鋅摻雜鎂、錳與鎘等元素之氧化鋅合金材料皆以此最佳品質之氧化鋅薄膜參數去成長。在氧化鎂鋅部分，成長出鎂濃度最高為11.2%之高品質氧化鎂鋅薄膜。此外，利用氧化鎂與氧化鋅兩層緩衝層以及熱退火方法可以改善氧化鎂鋅之薄膜的平整度。另一方面，我們也成功利用鎂濃度8.3%之氧化鎂鋅成長出氧化鋅/氧化鎂鋅量子井。

氧化錳鋅部分，成長出錳濃度最高為6.1%之高品質氧化錳鋅薄膜。在共振拉

曼光譜中我們發現氧化鋅樣品和氧化錳鋅樣品各自有5個和11個縱向光學聲子的訊號。藉由變溫共振拉曼光譜的實驗，可以得知縱向光學聲子訊號的強度與氧化錳鋅的能隙位置相關。除此之外，我們也對摻雜錳濃度0.3%的氧化錳鋅薄膜量測在磁場下的光激螢光光譜，在外加磁場5T時有9%的圓形極化率。

氧化鎘鋅部分，利用變溫光激螢光光譜與時間解析光激螢光光譜探討鎘濃度2%之氧化鎘鋅內部載子受熱效應影響下的躍遷行為。當基板溫度降低至350℃後，利用調控鎘與鋅的原子源流量比例即可成長出鎘含量為49.7%之高濃度且高品質之氧化鎘鋅薄膜。此系列的氧化鎘鋅薄膜的發光範圍涵蓋了可見光。此外也利用變溫光激螢光光譜探討載子在材料中受溫度影響後的躍遷行為。最後我們成長漸變濃度之氧化鎘鋅薄膜，利用光激螢光光譜與時間解析光譜量測技術定義出漸變濃度的氧化鎘鋅螢光的來源。除此之外，利用紅綠藍三色混光的的方法，此樣品發出的螢光在肉眼觀察下是白光而且室溫下材料的內部量子效率為33.67%。

Growth and Optical Study of High Quality ZnO, ZnMgO, ZnMnO and ZnCdO

Student：Kun-Feng Chien　　Advisor：Dr. Wu-Ching Chou

Institute of Electrophysics
National Chiao Tung University

Abstract

In this dissertation, the growth of high quality ZnO, ZnMgO, ZnMnO and ZnCdO thin films on Al_2O_3 substrate by plasma-assisted molecular beam epitaxy were studied. The photoluminescence (PL), transmittance and time-resolved photoluminescence (TRPL) were used to investigate the optical properties.

For the growth of $Zn_{1-x}Mg_xO$ (x=0~0.112) thin films, MgO buffer is used to improve the surface morphology during the initial growth stage, which eventually leads to an atomically flat surface. ZnO/ZnMgO multiple quantum wells were also fabricated successfully on the atomically flat MgO surface.

In the case of $Zn_{1-x}Mn_xO$ (x=0~0.061) thin films, transmittance spectra show an increase of band gap with the increasing Mn concentration. Resonant Raman scattering spectra showed 11 longitudinal optical phonon lines for the $Zn_{1-x}Mn_xO$ samples. In addition, circular polarization degree of 9 % was observed in the

$Zn_{0.997}Mn_{0.003}O$ sample at magnetic field B=5 T.

Furthermore, the growth of high quality $Zn_{1-x}Cd_xO$ thin films with visible light emission was achieved at growth temperature of 350 ℃. The concentration of Cd can be systematically adjusted via the Cd/Zn beam pressure ratio and the maximum concentration was 49.7 %. The origin of radiative recombination and dynamics of the charge carriers in the graded $Zn_{1-x}Cd_xO$ multilayers was investigated by means of PL and TRPL spectroscopy. The internal quantum efficiency of our sample achieved 33.67 %.

致謝(Acknowledgments)

當論文口試報告結束的那一刻，除了對於漫長的求學生涯畫下句點感到開心外，卻也莫名的感到接下來人生的另一個階段是要負起更多的責任。首先感謝論文指導教授周武清老師六年來的栽培與提供豐沛的資源。六年裡的過程可以算是辛苦的卻也非常充實。在研究上，除了參與國科會計畫外也參與過產學合作計畫，除了國內研討會外也有幾次機會到國外演討會見識，更有許多外國訪客的交流機會。在研究外的，除了參與實驗室重大的搬遷規劃也有機會到國外接受新儀器系統的受訓，還有許許多多與學弟妹相處的心得感想，其實也可以寫成另一本論文了。感謝大同大學楊祝壽老師，亦師亦友的楊老師是我這六年裡不論在研究上的問題或是生活中的瑣事都能無所不談的好老師好朋友。接著六年裡有許多協助我畢業的貴人來來往往，就讓我在這章節裡點名以示感謝：高雄大學謝振豪老師。實驗室學長李寧、文忠、瑞泰、怡仁、彥丞。學弟妹安傑、侑霖、維綸、蓉霏、偉仕、宣劭、湘穎、嘉華、詩涵、明皓、建德、悅如以及今年剛進來的碩一新生。外校生家偉、家興、高昆。此外，助理小育也幫實驗室攬下了許多行政上的事務，讓我能夠更專注在研究。以

上如果遺漏的請見諒，只要是曾在實驗室一起打拼努力的夥伴都是我的貴人。感謝女友慧娟及其家人在這六年來給過協助照顧與陪伴，最後當然是要感謝我的家人，有家人的支持才能讓我無後顧之憂的完成學業。在自己人生新一階段的展開，我將帶著一顆感恩的心，回饋所學。

Contents

Abstract (Chinese)……...i

Abstract (English)…….iii

Acknowledgements……v

Contents……...vii

Table captions…….viii

Figure captions…….....ix

Chapter 1 Introduction……1

Chapter 2 Experimental details……..5

Chapter 3 Growth and characterization of $Zn_{1-x}Mg_xO$ thin films and ZnO/ZnMgO multiple quantum wells……17

Chapter 4 Growth and optical properties of $Zn_{1-x}Mn_xO$ thin Films…….23

Chapter 5 Thermal-activated carrier transfer in $Zn_{0.98}Cd_{0.02}O$ thin film…….35

Chapter 6 Growth and carrier dynamics of $Zn_{1-x}Cd_xO$ thin films with visible light emission……44

Chapter 7 Optical properties of the graded $Zn_{1-x}Cd_xO$ film……..56

Chapter 8 Conclusion……76

Publications

Table captions

2.1 Growth conditions of ZnO thin films……10

2.2 Growth conditions of $Zn_{1-x}Mg_xO$ thin films……...10

2.3 Growth conditions of $Zn_{1-x}Mn_xO$ thin films……...11

2.4 Growth conditions of $Zn_{1-x}Cd_xO$ thin films……11

Figures captions

2.1 MBE system……...12

2.2 Growth rates of ZnO thin films as a function of Zn cell temperatures……..12

2.3 Low temperature (10 K) PL spectra of ZnO thin films with various Zn cell temperatures……...13

2.4 The intensity ratios of the NBE emission to the DL emission for ZnO thin films as a function of Zn cell temperatures……..13

2.5 Sample structure of $Zn_{1-x}Mg_xO$ thin films……....14

2.6 Sample structure of $Zn_{1-x}Mn_xO$ thin films……..14

2.7 Sample structure of $Zn_{1-x}Cd_xO$ thin films……...14

2.8 Experimental setup for the PL measurement……..15

2.9 Experimental setup for the transmittance measurement……16

2.10 Experimental setup for the TRPL measurement……...16

3.1 RHEED patterns show the surface morphology evolution during growth. **(a)** The Al_2O_3 (0001) surface after oxygen plasma treatment. **(b)** Growth of MgO buffer layer starts. **(c)** and **(d)** respectively correspond to ZnO surfaces before and after annealing……20

3.2 PL spectra of the $Zn_{1-x}Mg_xO$ films ($0 \leqq x \leqq 0.112$) at 10 K. The inset shows the transmittance spectra of $Zn_{1-x}Mg_xO$ at 10 K……..21

3.3 PL spectra from the series of ZnO/ $Zn_{0.917}Mg_{0.083}O$ QWs recorded at 10 K. The QW thickness varies from 2.0 to 3.5 nm…….....22

4.1 **(a)** Room temperature transmittance spectra of $Zn_{1-x}Mn_xO$ thin films with Mn concentration x=0, 0.009, 0.030 and 0.061. **(b)** The energy of absorption edge for $Zn_{1-x}Mn_xO$ thin films as a function of the Mn concentrations(x). The experimental results of ours(□) and reference 24 (■) are plotted……30

4.2 Resonant Raman scatterings of ZnO and $Zn_{0.97}Mn_{0.03}O$ thin films, using the He–Cd laser (λ=325 nm)……31

4.3 Resonant Raman scatterings of $Zn_{1-x}Mn_xO$ thin films, using the He–Cd laser (λ=325 nm)……32

4.4 **(a)** Resonant Raman scatterings of $Zn_{0.991}Mn_{0.009}O$ thin films with variable temperature, using the He-Cd laser (λ = 325 nm). The arrows show the PL positions. **(b)** Temperature dependent PL position of $Zn_{0.991}Mn_{0.009}O$. The solid curve describes the fit of these data by using the Bose-Einstein statistical factor for phonons. The dashed lines represents the energy positions of the scattered photons with energy $\hbar\omega \cong \hbar\omega_i - n\hbar\omega_{LO}$, n = 6 or 7……..33

4.5 Low temperature (10 K) PL spectra of $Zn_{0.997}Mn_{0.003}O$ for B = 0 and B = 5 Tesla……....34

5.1 PL spectra of ZnO and $Zn_{0.98}Cd_{0.02}O$ films at10 K. The inset shows the PL and

transmittance spectra of $Zn_{0.98}Cd_{0.02}O$ at 10 K……...40

5.2 PL spectra of **(a)** ZnO and **(b)** $Zn_{0.98}Cd_{0.02}O$ thin films at various temperatures. **(c)** Integrated PL intensity of X/Cd_n as a function of temperature for $Zn_{0.98}Cd_{0.02}O$. The solid line is fitted by Eq. (1)……41

5.3 **(a)** PL peak energy trace of X/Cd, X/Cd_n, X/Cd cluster and FX at various temperatures. The solid lines are Varshni's fits. **(b)** Power dependent spectra of $Zn_{0.98}Cd_{0.02}O$ at 220 K……42

5.4 Temporal evolution of the PL spectra at **(a)** 10 K, **(b)** 100 K, and **(c)** 150 K……43

6.1 Cd content increases linearly with the increasing Cd/Zn beam pressure ratio. The inset shows the RHEED pattern of $Zn_{0.503}Cd_{0.497}O$ taken along the (11-2) azimuth……...51

6.2 **(a)** PL spectra of the $Zn_{1-x}Cd_xO$ films ($0 \leqq x \leqq 0.497$) at 10 K. **(b)** PL peak energy of $Zn_{1-x}Cd_xO$ as a function of Cd content x……52

6.3 PL spectra of $Zn_{1-x}Cd_xO$ with x= 0.062, 0.185, 0.366 and 0.454 at various temperatures……...53

6.4 **(a)** PL peak energy of $Zn_{0.938}Cd_{0.062}O$, $Zn_{0.815}Cd_{0.185}O$, and $Zn_{0.634}Cd_{0.366}O$ at various temperatures. The dotted line is the Varshni's fit. **(b)** Integrated PL intensity as a function of temperature for $Zn_{0.938}Cd_{0.062}O$, $Zn_{0.815}Cd_{0.185}O$, and $Zn_{0.634}Cd_{0.366}O$. **(c)** Integrated PL intensity as a function of temperature for the

$Zn_{0.634}Cd_{0.366}O$. The dotted line is fitted by Eq. (4)……55

7.1 **(a)** Growth profile of $Zn_{1-x}Cd_xO$ structures and schematic graded band gap diagram. **(b)** PL spectra of the graded $Zn_{1-x}Cd_xO$ film at 10 K……..62

7.2 PL spectra of the graded $Zn_{1-x}Cd_xO$ film at10 K. The spectrum range is from 1.40 eV to 3.2 eV and the dotted-lines were curve fitting to the spectrum. **(b)** PL and transmittance spectra of the graded $Zn_{1-x}Cd_xO$ film at 10 K……..63

7.3 **(a)** PL spectra of the graded $Zn_{1-x}Cd_xO$ and the $Zn_{0.741}Cd_{0.259}O$ at 10 K. The inset shows the PL spectra with log scale. **(b)** Transmittance spectra of the graded $Zn_{1-x}Cd_xO$ and the $Zn_{0.741}Cd_{0.259}O$ at 10 K. **(c)** PL spectra obtained at 10 K from the graded $Zn_{1-x}Cd_xO$ using different excitation (325 nm and 377 nm). **(d)** White PL emission can be observed by naked eye……...65

7.4 PL spectra of the graded $Zn_{1-x}Cd_xO$ film at various temperatures. The inset shows integrated PL intensities as a function of temperature for the graded $Zn_{1-x}Cd_xO$ film……66

7.5 **(a)** PL intensity decay as a function of temperature. **(b)** PL decay time and stretching exponent (β) of graded $Zn_{1-x}Cd_xO$ as a functions of temperature. **(c)** Temperature dependence of measured PL decay time along with the extracted radiative and nonradiative lifetime parameters. The transition temperature T_{TR} is indicated by an arrow……69

Chapter 1

Introduction

Recently, ZnO-based optoelectronic devices have attracted increasing attentions due to their attractive properties of the wide band gap (3.37 eV) and high exciton binding energy (60 meV) [1]. In addition, ZnO has certain advantages, including the availability of fairly high quality ZnO bulk single crystals and the amenability to wet chemical etching [2-4]. For the development of ZnO-based optoelectronic devices, such as light emitting diodes, solar blind photo detectors, and transparent thin film transistors [5-9], the growth of high quality ZnO-based ternary compounds and quantum well structures is crucial. Molecular beam epitaxy (MBE) is one of best growth techniques to grow such structures. MBE operates in ultra-high vacuum condition, which allows a slow deposition rate and the observation of in-situ growth by reflection high energy electron diffraction (RHEED). By this way, films and quantum structures of high quality could be grown. In addition, many molecular sources can be installed in a typical MBE system. As a result, novel binary, ternary and quaternary compound semiconductors with good crystal quality can be prepared. In this thesis, MBE technique was used to grow the ZnO, $Zn_{1-x}Mg_xO$, $Zn_{1-x}Mn_xO$ and $Zn_{1-x}Cd_xO$. The optical properties of these materials were studied.

In chapter 2, the MBE growth technique was described. The optical spectroscopy, which includes the photoluminescence, transmittance, and time-resolved photoluminescence used to investigate the optical properties were presented. The growth conditions of all samples in this thesis were also shown.

In chapter 3, ZnO and $Zn_{1-x}Mg_xO$ epitaxial films were grown on *c*-plane sapphire substrates using MgO buffer layers. Presently, sapphire is the most commonly used substrate for ZnO-based epitaxial growth. Since sapphire has the advantages of thermal stability at high growth temperature, chemical inertness, strong bond strength. However, the lattice mismatch between ZnO and sapphire is 18.4 % [10]. For that reason, the ZnO films generally show rough surface morphology and poor crystal quality when ZnO films are directly grown on *c*-plane sapphire substrates without a buffer layer. MgO is the most widely used buffer layer for ZnO grown on sapphire substrates, because the lattice mismatch between ZnO and MgO reduce to 8.4 % [11]. Nowadays, the wavelength for emission or detection can be tuned by using either ZnO quantum well or by alloying ZnO with a higher band gap material. MgO has a band gap of about 6.7 eV. Though the equilibrium solid solubility of MgO in ZnO in the bulk form is limited (less than 4 mol. %), but the ionic radii of Mg^{2+} (0.057 nm) is similar to that of Zn^{2+} (0.060 nm) [12]. Since MBE is a non-equilibrium processing technique, solid solubility of MgO in ZnO can be significantly enhanced in

the metastable state after thin film deposition. Thus, we report the growth and optical properties of ZnO and $Zn_{1-x}Mg_xO$ thin films grown on *c*-plane sapphire substrates using MgO buffer layers in this thesis.

In chapter 4, the growth and optical property of $Zn_{1-x}Mn_xO$ thin film was described. Diluted magnetic semiconductors (DMS) have been intensely studied in the last few decades. By introducing the magnetic atoms to substitute the cations of the binary semiconductors, such as II-VI or III-V compound semiconductors, the band gaps can be varied and the semiconductors also exhibit very interesting magnetic effects [13]. Among II-VI DMS, $Zn_{1-x}Mn_xO$ has direct band gap (above 3.37 eV at 300 K) and large exciton binding energy (near 60 meV). Furthermore, Mn^{2+} ion has half-filled 3*d*-orbital with five electrons in the same spin direction, therefore it has the large total spin angular momentum (S = 5/2). These advantages make $Zn_{1-x}Mn_xO$ a potential material for applications in spintronics such as spin light-emitting diodes (spin LEDs) and spin filters. Recently, there are some papers focused on the magnetic properties of ZnMnO because of the prediction of room temperature ferromagnetism [14], however optical properties of ZnMnO are still rarely studied. Therefore, in this thesis, resonant Raman scattering and photoluminescence of ZnMnO with variant Mn concentration are investigated.

In chapter 5, 6 and 7, the growth and optical properties of $Zn_{1-x}Cd_xO$ thin films

were depicted. For visible emission, $Zn_{1-x}Cd_xO$ is a suitable compound for extending emission wavelength from ultraviolet to blue and green spectral regions owing to the smaller band gap of CdO of 2.3 eV [15]. In addition, the fabrication of ZnO/$Zn_{1-x}Cd_xO$ heterojunctions and multiple quantum wells would provide the key element in ZnO-based light emitting diodes and laser diodes. However, the rock-salt structure of CdO is dissimilar to the wurtzite structure of ZnO, which induces problems for ZnCdO alloys, such as poor crystalline quality. Up to date, $Zn_{1-x}Cd_xO$ film had been recently prepared by pulse-laser deposition [16], metal organic chemical vapor deposition (MOCVD) [17-18], and MBE [19]. In comparison, MBE distinguished by its high versatility and the capability of in situ growth control. However, the results about the fabrication and optical properties of $Zn_{1-x}Cd_xO$ films grown by MBE are still rather limited. Sadofev *et al.* [19] demonstrated single-phase $Zn_{1-x}Cd_xO$ layers with Cd composition up to 32 % by MBE. Although, the Cd composition in $Zn_{1-x}Cd_xO$ films exceeds x=32 %, which is much less than that was grown by MOCVD (69 %) [18]. Therefore, in chapter 5, 6 and 7, we represent the growth approaches to fabricate high quality $Zn_{1-x}Cd_xO$ films with high Cd concentration and visible light emission using MBE. Detailed studies of temperature dependent PL and TRPL of $Zn_{1-x}Cd_xO$ films with different concentration of Cd are also reported. Finally, a brief conclusion will be presented in chapter 8.

Chapter 2

Experimental details

In this chapter, the experimental techniques used in this thesis were described. The experimental techniques include plasma-assisted molecular beam epitaxy (PA-MBE), photoluminescence (PL) spectroscopy, transmittance (T), time-resolved photoluminescence spectroscopy (TRPL). The growth conditions of all samples will be listed.

2.1 MBE system

The SVT Associates MBE system is shown in Fig. 2.1. It consists of a vertical growth chamber with ten cell ports, a load-lock chamber, and analytical equipments.

Currently, six solid sources Zn, Mn, Cd, Mg, Se, Te, and gas source (Oxygen), are installed in the effusion cells and plasma cell. Each source has its own shutter to control the supply duration of each source. The samples were grown on the heated substrate which was set to rotate for uniform growth and there is a main-shutter between sources and the substrate to avoid the unintentional evaporation before growth.

The load-lock chamber is used to transfer substrate from air to the growth

chamber. Its high vacuum (< 5×10^{-8} torr) is achieved by using a diaphragm pump and a turbo pump. The growth chamber was further pumped down to a base pressure of 2×10^{-10} torr. The reflection high-energy electron diffraction (RHEED) system is also set up in the growth chamber. It is an invaluable tool to determine different aspects of the deposition layer. Morphological data of the surface may be interpreted from the spot and line pattern, which appear on the phosphor screen display during growth.

2.2 Growth conditions of ZnO

The detailed growth conditions of ZnO thin films are listed in Table 2.1. Fig. 2.2 shows the growth rates of ZnO thin films with various Zn cell temperatures. When the substrate temperature was fixed at 650 ℃ and the oxygen flow rate was 0.6 SCCM with plasma power 250 W, the growth rate increases linearly with the increasing Zn cell temperature, which indicates these ZnO thin films were grown under oxygen-rich conditions.

The PL spectra of ZnO thin films with various Zn cell temperatures at 10 K are shown in Fig. 2.3. For these samples, the dominant peaks around 3.36 eV are attributed to the near band edge (NBE) emission [20]. The broad and weak emissions which originate from the deep levels (DLs) near 2.25 eV are also observed. The DLs are attributed to the zinc interstitial (Zn_i), oxygen vacancy (V_o) [21], and oxygen interstitial (O_i) [22]. Fig. 2.4 shows the intensity ratios of the NBE emission to the DL

emission. The intensity ratio reaches maximum value of 75 at Zn cell temperature of 280 ℃. This growth condition was used for the growth of $Zn_{1-x}Mg_xO$, $Zn_{1-x}Mn_xO$ and $Zn_{1-x}Cd_xO$ epilayers.

2.3 Growth condition of $Zn_{1-x}Mg_xO$

The structure of the $Zn_{1-x}Mg_xO$ thin films used in chapter 3 was shown in Fig. 2.5. The detailed growth conditions of $Zn_{1-x}Mg_xO$ thin films are listed in Table 2.2.

2.4 Growth condition of $Zn_{1-x}Mn_xO$

The structure of the $Zn_{1-x}Mn_xO$ thin films used in chapter 4 was shown in Fig. 2.6. The detailed growth conditions of $Zn_{1-x}Mg_xO$ thin films are listed in Table 2.3.

2.5 Growth condition of $Zn_{1-x}Cd_xO$

The structure of the $Zn_{1-x}Cd_xO$ thin films used in chapter 5~7 was shown in Fig. 2.7. The detailed growth conditions of $Zn_{1-x}Cd_xO$ thin films are listed in Table 2.4.

2.6 Photoluminescence spectroscopy

To study optical properties of semiconductors, laser beams with photon energy higher than the band gap energy of the semiconductor are usually used to excite electrons from the valence band to the conduction band and leave holes in the valence band. The excited electrons/holes relaxed to the bottom of conduction band/top of the valence band through the carrier-phonon interaction. Electron and hole pair forms

exciton by Coulomb interaction. Electrons and holes, Excitons, recombine and emit photons. The emitted photons can be detected and analyzed by photoluminescence (PL) spectroscopy.

The experimental set-up for the PL measurement is shown in Fig. 2.8. PL measurements were performed by using the 325 nm line of a He-Cd laser. The incident beam was focused by a lens (f=10 cm). The PL emission from sample was collected by second lens (f=10 cm) and focused by the third lens (f=30 cm) to the spectrometer. The signal was dispersed by an *i*HR550 spectrometer and detected by liquid nitrogen cooled charge-coupled device (CCD). The spectrometer was controlled by a computer, which was used to store and plot the collected data. For temperature-dependent PL measurements, samples were cooled in a closed-cycle refrigerator system. The temperature was varied from 10 K to 300 K.

2.7 Transmittance

The experimental set-up for transmittance measurement is shown in Fig. 2.9. A broadband xenon lamp was used as an excitation source. The incident beam was focused on the sample by a lens (f=10 cm). The transmittance beam from the sample was collected to the entrance slit by lens L2 (f=10 cm) and L3 (f=30 cm). The transmittance spectra were analyzed by the *i*HR550 spectrometer and detected by

liquid nitrogen cooled charge-coupled device.

2.8 Time-resolved photoluminescence spectroscopy

TRPL system was used to study the decay dynamics of excitons. The experimental setup of TRPL system is similar to the PL system and shown in Fig. 2.10. The GaN diode laser with 50 ps pulses and a repetition rate of 40 MHz at a wavelength of 377 nm was used as an excitation source. The peak power of the pulse was estimated to be below 0.1 mW. The laser beam was focused on the sample by a lens (f=10 cm). The combination lenses guide the signal to the iHR550 spectrometer, which was equipped with a high-speed photomultiplier tube to detect the signal. The signal was further analyzed by a computer. The overall temporal resolution of the setup was about 300 ps.

	T (substrate) (℃)	T (Zn) (℃)	O_2 plasma (SCCM/W)	Thickness (nm)
Sample 1-A	650	270	0.6/250	131
Sample 1-B	650	275	0.6/250	144
Sample 1-C	650	280	0.6/250	159
Sample 1-D	650	285	0.6/250	181
Sample 1-E	650	290	0.6/250	225

Table 2.1 Growth conditions of ZnO thin films.

	T (substrate) (℃)	T (Zn) (℃)	O_2 plasma (SCCM/W)	T (Mg) (℃)	$Zn_{1-x}Mg_xO$ (x)
Sample 2-A	650	280	0.6/250	290	0.033
Sample 2-B	650	280	0.6/250	300	0.064
Sample 2-C	650	280	0.6/250	310	0.083
Sample 2-D	650	280	0.6/250	320	0.112

Table 2.2 Growth conditions of $Zn_{1-x}Mg_xO$ thin films.

	T (substrate) (℃)	T (Zn) (℃)	O_2 plasma (SCCM/W)	T (Mn) (℃)	$Zn_{1-x}Mn_xO$ (x)
Sample 3-A	650	280	0.6/250	680	0.003
Sample 3-B	650	280	0.6/250	700	0.009
Sample 3-C	650	280	0.6/250	720	0.011
Sample 3-D	650	280	0.6/250	730	0.021
Sample 3-E	650	280	0.6/250	735	0.026
Sample 3-F	650	280	0.6/250	740	0.030
Sample 3-G	650	280	0.6/250	760	0.039
Sample 3-H	650	280	0.6/250	770	0.061

Table 2.3 Growth conditions of $Zn_{1-x}Mn_xO$ thin films.

	T (substrate) (℃)	T (Zn) (℃)	O_2 plasma (SCCM/W)	T (Mn) (℃)	$Zn_{1-x}Cd_xO$ (x)
Sample 4-A	650	280	0.6/250	180	0.062
Sample 4-B	650	280	0.6/250	190	0.104
Sample 4-C	650	280	0.6/250	195	0.185
Sample 4-D	650	280	0.6/250	200	0.256
Sample 4-E	650	280	0.6/250	210	0.366
Sample 4-F	650	280	0.6/250	220	0.454
Sample 4-G	650	280	0.6/250	230	0.497

Table 2.4 Growth conditions of $Zn_{1-x}Cd_xO$ thin films.

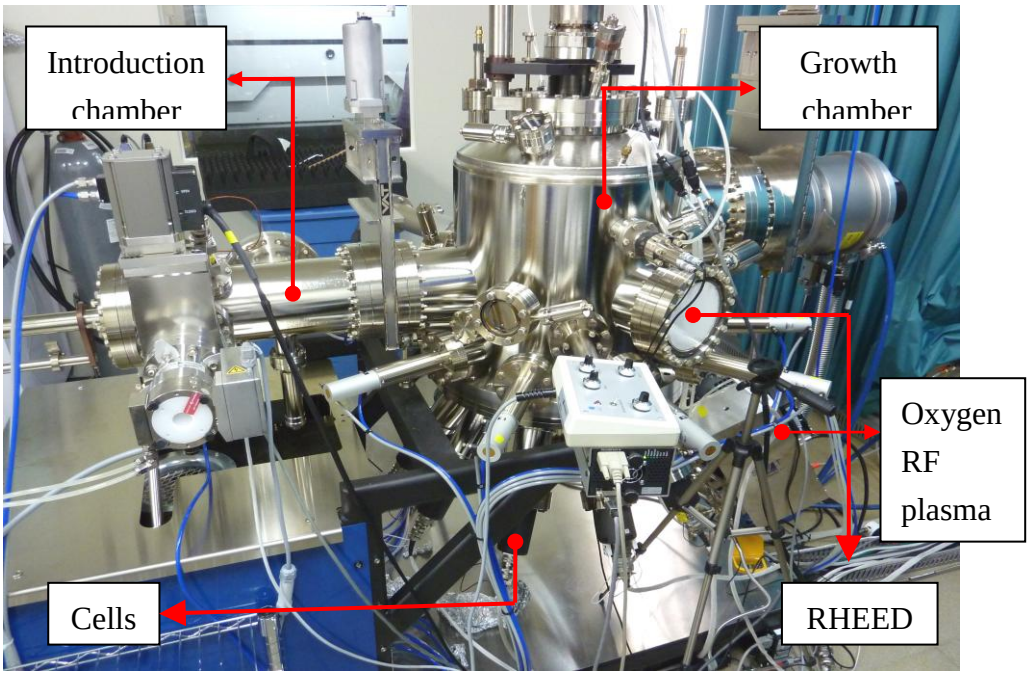

Fig. 2.1 MBE system.

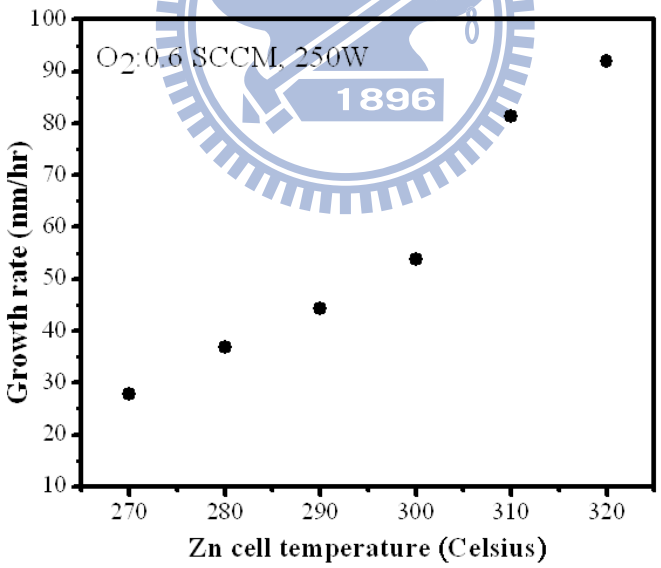

Fig. 2.2 Growth rates of ZnO thin films as a function of Zn cell temperatures.

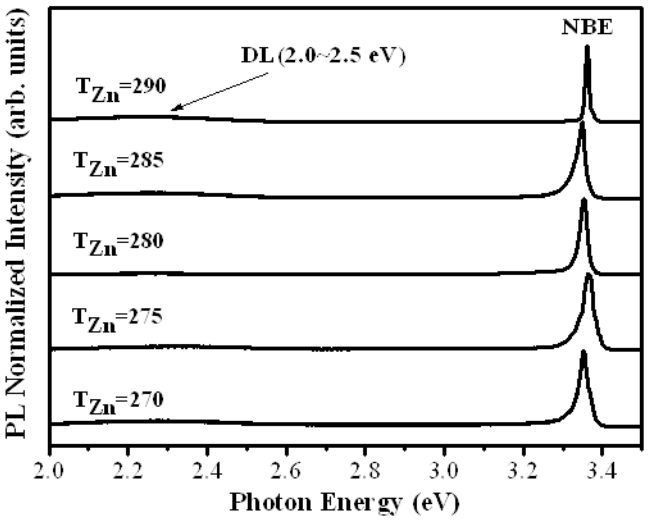

Fig. 2.3 Low temperature (10 K) PL spectra of ZnO thin films with various Zn cell temperatures.

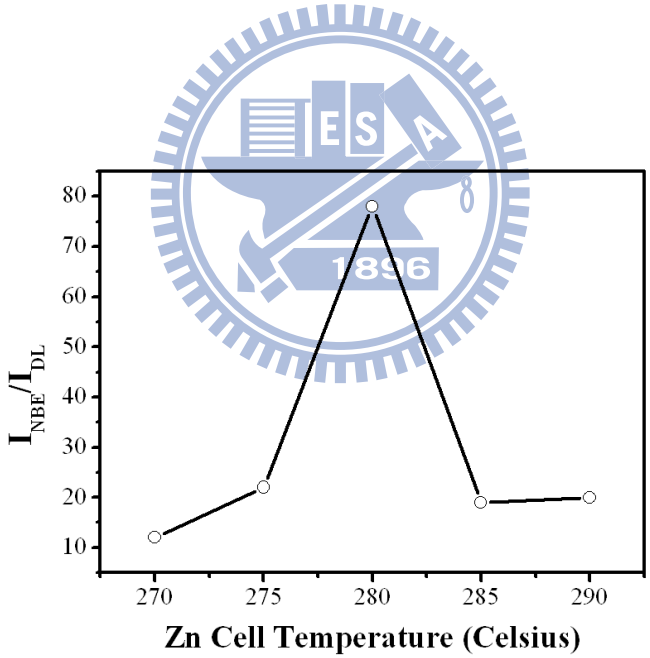

Fig. 2.4 The intensity ratios of the NBE emission to the DL emission for ZnO thin films as a function of Zn cell temperatures.

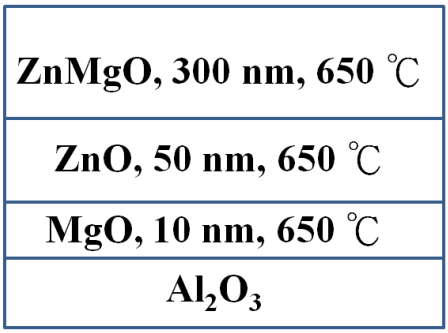

Fig. 2.5 Sample structure of $Zn_{1-x}Mg_xO$ thin films.

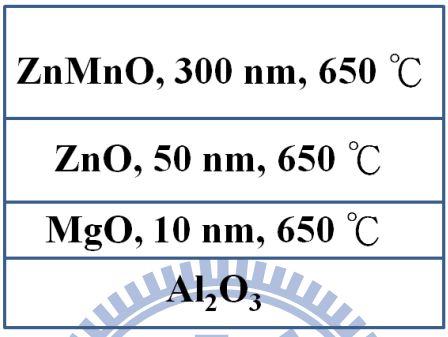

Fig. 2.6 Sample structure of $Zn_{1-x}Mn_xO$ thin films.

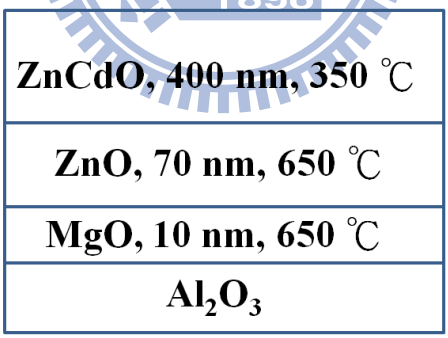

Fig. 2.7 Sample structure of $Zn_{1-x}Cd_xO$ thin films.

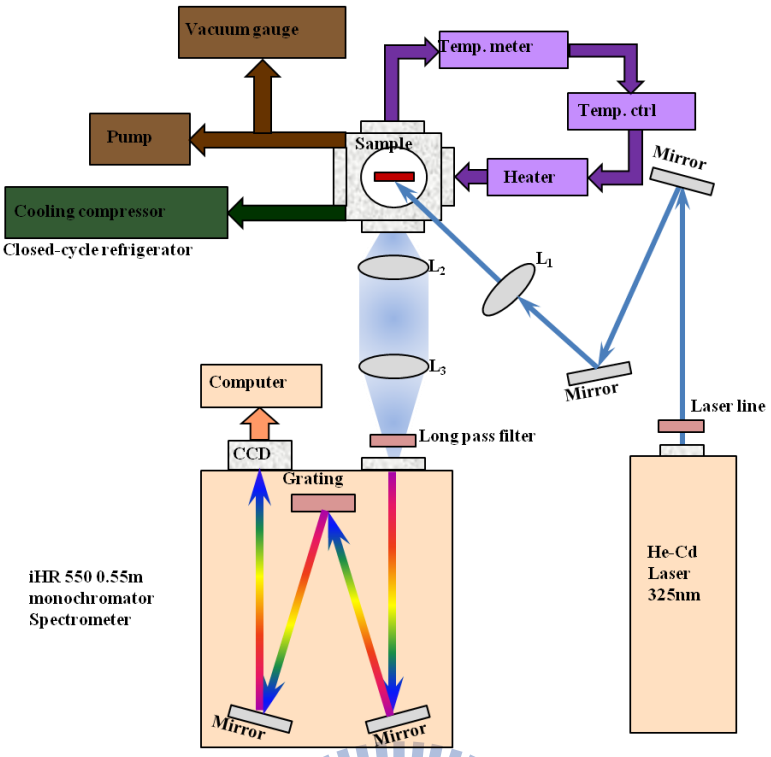

Fig. 2.8 Experimental setup for the PL measurement.

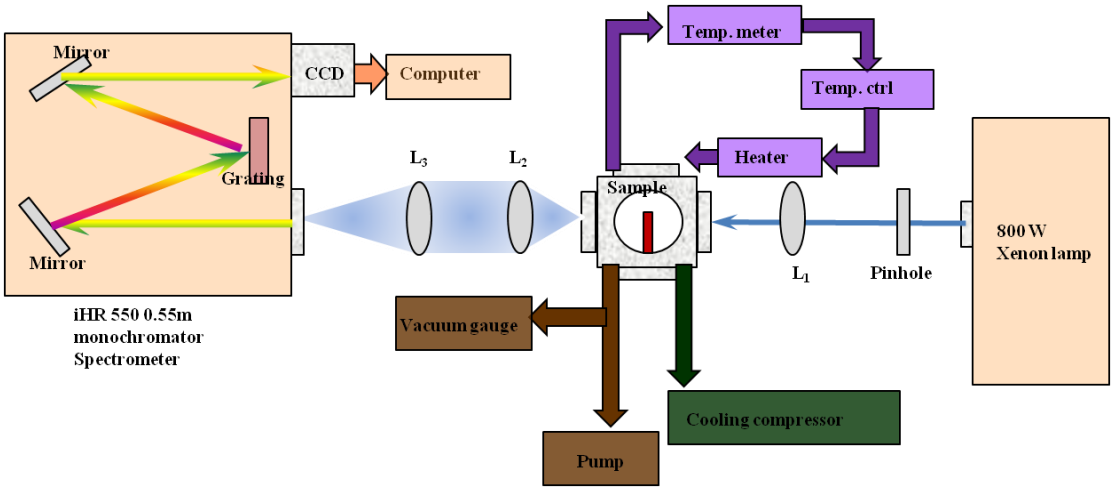

Fig. 2.9 Experimental setup for the transmittance measurement.

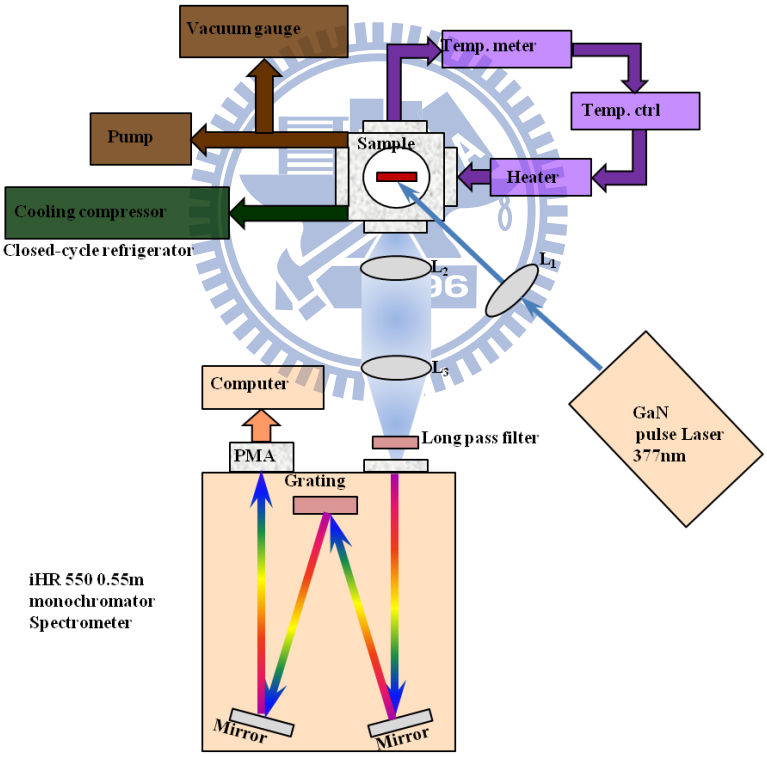

Fig. 2.10 Experimental setup for the TRPL measurement.

Chapter 3

Growth and characterization of $Zn_{1-x}Mg_xO$ thin films and ZnO/ZnMgO multiple quantum wells

In this chapter, growth and characterization of $Zn_{1-x}Mg_xO$ (x=0~0.112) thin films grown by molecular beam epitaxy system will be discussed. The MgO buffer is very useful for the improvement of surface morphology during the initial growth stage, which eventually leads to an atomically flat surface. Additionally, ZnO/ZnMgO multiple quantum wells (QWs) were also fabricated successfully and their optical properties were investigated.

The morphology evolution can be observed by *in situ* reflection high-energy electron diffraction (RHEED). At the beginning of MgO deposition, the sharp streaky pattern of clean Al_2O_3 substrate~~s~~, as shown in Fig. 1 (a), becomes diffuse spotty pattern, as shown in Fig. 1 (b), because of the large (8%) lattice mismatch between MgO(111) and Al_2O_3 (0001). Therefore, the growth of MgO is a 3-dimensional growth mode. Immediately after the growth of MgO buffer layer, the ZnO growth starts with spotty patterns, as shown in figure 1 (c), superimposing on the MgO patterns with the spot spacing about 9% smaller. As the growth continues, the RHEED spots gradually elongate and finally become streaks. This self-flattening

procedure can be dramatically accelerated by interrupting the deposition and annealing the sample at 750 ℃. After 5 min annealing, Fig. 1(d) shows sharp streaky RHEED patterns of ZnO. Thus, a flat surface of buffer layer was accomplished. The growth of $Zn_{1-x}Mg_xO$ epilayers then starts at 650 ℃, with the same oxygen flow rate of 0.6 sccm under the plasma power of 250 W as MgO and ZnO buffers. The Zn cell temperature is 280℃ and the Mg cell temperatures are varied from 290 to 300, 310, and 320℃ for the growth of $Zn_{1-x}Mg_xO$ thin films.

In this study, the Mg content in $Zn_{1-x}Mg_xO$ was determined by energy dispersive x-ray spectroscopy. Fig. 2 shows the PL spectra of the $Zn_{1-x}Mg_xO$ layers recorded at a temperature of 10 K exhibit a sharp band edge luminescence, which originates from the recombination of bound excitons. The emission spectra of $Zn_{1-x}Mg_xO$ films ~~is~~ broadened due to alloying and the related potential fluctuations. Additionally, the emissions which originate from the deep levels near 2.25 eV are not observed. For increasing Mg content the excitonic luminescence exhibits blue shift. The maximum emission energy is 3.71 eV for the $Zn_{0.888}Mg_{0.112}O$ sample. he low-temperature transmittance spectra of $Zn_{1-x}Mg_xO$ are also shown in the inset of Fig. 2. The energy of strong absorption edge increases with Mg concentration. It implies the growth of high quality $Zn_{1-x}Mg_xO$ thin films with MgO/ZnO buffer layers were achieved.

Finally, the conditions of high quality $Zn_{0.917}Mg_{0.083}O$ thin film was used to grow

the ZnO/ $Zn_{0.917}Mg_{0.083}O$ multiple QWs. Fig. 3 displays the low-temperature (10K) PL spectra from the series of QWs with well width from 2.0 to 3.5 nm. The emission of a donor-bound exciton at 3.36 eV from the ZnO well is clearly identified. The decrease in emission energy with the increasing well width is owing to the confinement effect. Additionally, the full width at half maximum of the PL emission from the ZnO well with 2 nm(~50 meV) is narrower than previous reports(~60 meV) [23]. Thus the quality of ZnO/ZnMgO multiple QWs is comparable to that was used to fabricate ZnO/ZnMgO multiple QW based high-efficiency light emitting diodes.

In conclusion, high quality $Zn_{1-x}Mg_xO$ (x=0~0.112) thin films were grown by PA-MBE. The MgO buffer is very effective for the improvement of surface morphology during the initial growth stage, which eventually leads to an atomically flat surface. The energy of absorption edge increasing with Mg concentration was observed. Additionally, high quality ZnO/ZnMgO multiple QWs were also fabricated.

(a) (b) (c) (d)

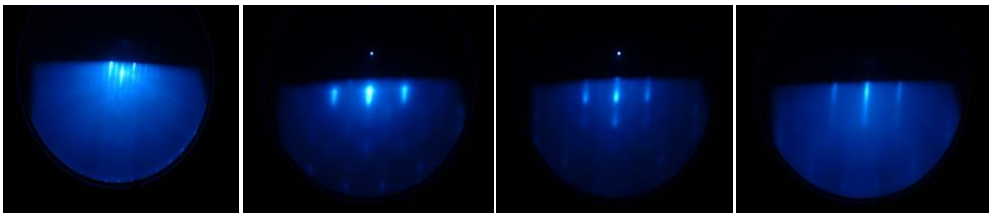

Fig. 1 RHEED patterns show the surface morphology evolution during growth. **(a)** The Al_2O_3 (0001) surface after oxygen plasma treatment. **(b)** Growth of MgO buffer layer starts. **(c)** and **(d)** respectively correspond to ZnO surfaces before and after annealing.

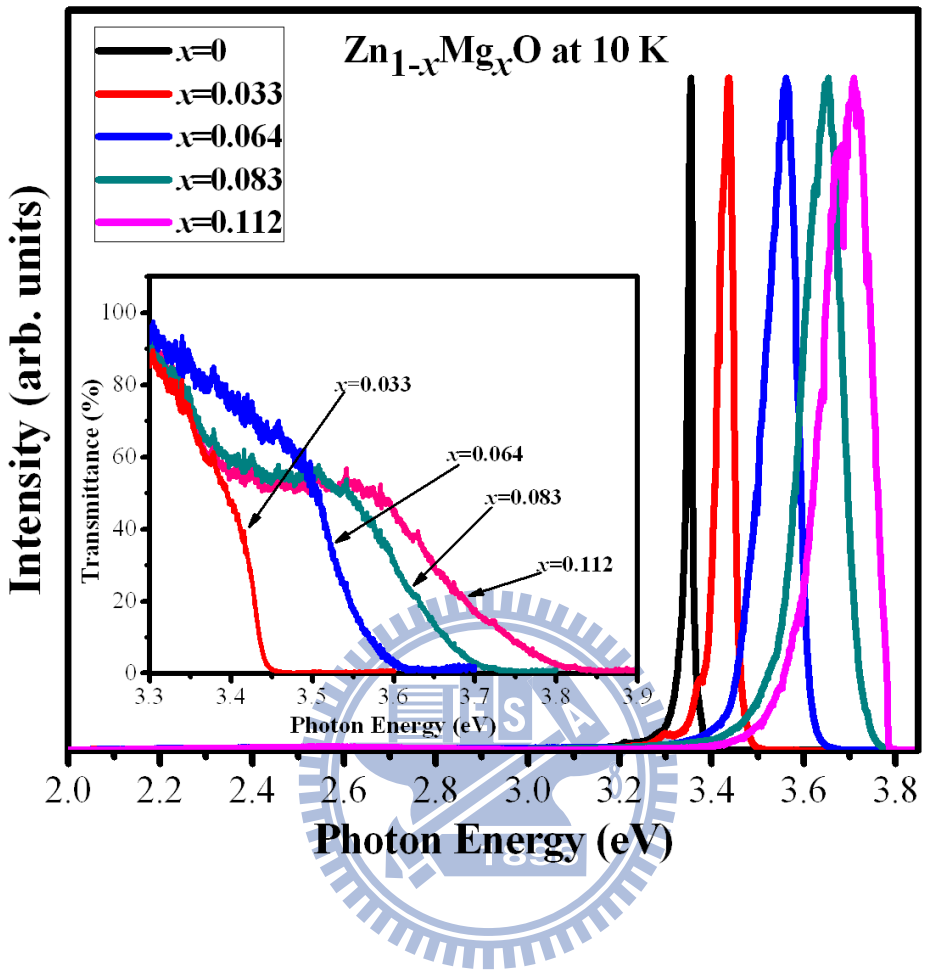

Fig. 2 PL spectra of the $Zn_{1-x}Mg_xO$ films ($0 \leqq x \leqq 0.112$) at 10 K. The inset shows the transmittance spectra of $Zn_{1-x}Mg_xO$ at 10 K.

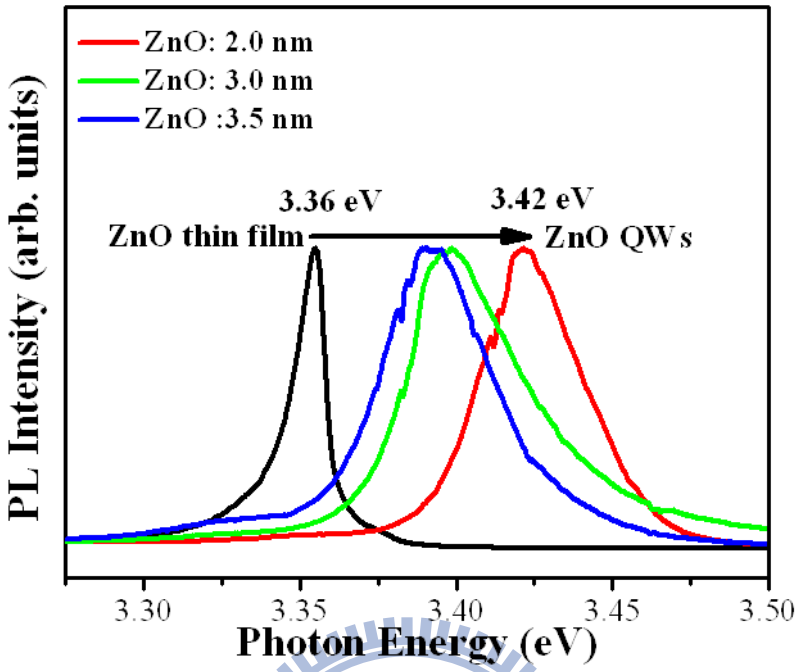

Fig. 3 PL spectra from the series of ZnO/ $Zn_{0.917}Mg_{0.083}O$ QWs recorded at 10 K. The QW thickness varies from 2.0 to 3.5 nm.

Chapter 4

Growth and optical Properties of $Zn_{1-x}Mn_xO$ thin Films

In this chapter, optical properties of $Zn_{1-x}Mn_xO$ (x=0~0.061) thin films will be studied by transmittance, resonance Raman scattering and circular polarization measurements.

Figure 1(a) shows room temperature transmittance spectra of $Zn_{1-x}Mn_xO$ thin films with Mn concentration x=0, 0.009, 0.030 and 0.061. The absorption edge energy increasing with Mn concentration can be observed. Additionally, the absorption edge broadening is assumed as E(band-maximum) - E(absorption edge). The broadening is because of the generation of disorder in the semiconductor, this causes some localized states [24]. Compared with the absorption edge broadening published in some papers (from 90 to 140 meV) [25-26], the absorption edge broadening of our samples (from 20 to 35 meV) are narrower. It means that there is high quality in our samples. Figure 1(b) shows the absorption edge energy of the $Zn_{1-x}Mn_xO$ versus Mn concentration. The blue shift of the absorption energy is due to MnO having a larger band gap than ZnO [27]. The shift of the absorption edge can be expressed by the following equation

$$E(x) = 3.337 + 3.056\,x(eV) \qquad (1).$$

The experimental results are in good agreement with reference 24. Furthermore, the

broadening of the absorption edge increases with the Mn concentration. The broadening is mainly due to the increasing disorder with increasing Mn concentration in $Zn_{1-x}Mn_xO$. There are also strong mid-gap absorptions around 3 eV for higher Mn concentration samples. This effect has been ascribed to the transition involves *d* orbital of the Mn^{2+} ion [28].

Figure 2 shows low temperature (10 K) resonant Raman scattering (RRS) spectra of ZnO and $Zn_{0.97}Mn_{0.03}O$ thin films using the He-Cd laser (λ=325 nm) excitation. RRS experiment is performed under the excitation laser energy higher than the band gap, and the incident photon energy will be in resonance with the electronic interband transition. The peak at 578 cm^{-1} is the first-order longitudinal optical (LO) phonon mode [29], in which both O and Zn atoms vibrate in the same direction. The weak peak around 457 cm^{-1} is ascribed to the E_2 (high) mode. Compared with 440 cm^{-1} in bulk ZnO single crystal [29], the frequency of the E_2 (high) mode in our sample is slightly larger, it is mainly due to strain effect in the thin film. Under RRS condition, some intense peaks at frequency positions of approximately integer times 578 cm^{-1} contribute to the *n*th-order LO phonon scattering processes. These are intense LO phonon lines because of the Frohlich interaction, which is the interaction between electrons and the longitudinal electrical field induced by the LO phonons [30]. In addition, there are also some relatively weak peaks at frequency positions next to

these LO phonon modes. Interestingly, the intervals of these weak peaks are also close to the frequency of LO phonon mode. Considering the frequency positions of these peaks, they are probably caused by the combination of E_2 (high) mode and multiple LO phonon scattering.

From the RRS spectra, we find 5 and 11 LO phonon modes for ZnO and $Zn_{0.97}Mn_{0.03}O$ samples, respectively. In previous studies [31], J. F. Scott *et al* reported that the LO phonon numbers (n) in RRS spectra varies proportionally with the electron-phonon coupling coefficient (α), which is given as the ratio of the Frohlich interaction energy to the LO phonon energy. They also predicted the number of LO phonon modes in ZnO is more than $n=9$ in CdS. However, they only found $n=8$ in their ZnO sample. From our results, we could not find LO phonon lines for $n>5$ in ZnO due to the strong near band edge PL emission. However, for $Zn_{0.97}Mn_{0.03}O$, the near band edge emission is weak and due to the large electron-phonon coupling coefficient $\alpha=0.9$ (is assumed to be the same as ZnO), the observation of large amount of LO phonon lines ($n=11$) in RRS spectra can be understood.

Figure 3 shows the RRS spectra of $Zn_{1-x}Mn_xO$ (x=0.003~0.030) thin films. Besides some intense LO phonon lines, there is an extra peak at 3632 cm^{-1} for $Zn_{0.997}Mn_{0.003}O$ sample. This peak is ascribed to the neutral donor bound exciton (D_0X) emission. As shown in the spectra, the LO phonon mode intensity at the

frequency position of around 3500 cm^{-1}, which is assigned to the sixth-order LO phonon mode, is always the largest in each of $Zn_{1-x}Mn_xO$ samples, and the intensity decreases with increasing Mn concentration. The behavior of intensity variation is mainly related to the band gap position, and it can be explained by using the Raman cross section for the *n*th-order LO phonon mode which is given as [32]

$$\sigma_n(\omega) = \mu^4 \sum_{j=0}^{\infty} \left| \sum_{m=0}^{\infty} \frac{\langle g, n+j | e, m \rangle \langle e, m | g, j \rangle}{E_{ex} + (m-j)\hbar\omega_{LO} - \hbar\omega_i + i\hbar\Gamma} \right|^2 \exp\left(-\frac{j\hbar\omega_{LO}}{k_B T} \right) \quad (2),$$

where μ is the electronic transition dipole moment, E_{ex} is the electronic transition energy. $\hbar\omega_i$ and $\hbar\omega_{LO}$ are the energies of the incident photon and the LO phonon, respectively. Γ is the homogeneous line width. $|g, n+j\rangle$ and $|g, j\rangle$ are the (*n*+*j*) th-order and *j*th-order LO phonon states in the electronic ground state, respectively. $|e, m\rangle$ is the *m*th-order LO phonon state in the electronic excited e state. k_B is Boltzmann's constant and *T* is the temperature. From this equation, the *n*th-order LO phonon mode intensity will become larger if $E_g \cong \hbar\omega_i - n\hbar\omega_{LO}$. The band gap of $Zn_{1-x}Mn_xO$ shifts to higher energy when Mn concentration increases, and it tends to be away from the frequency position of around 3500 cm^{-1}. Therefore, the intensity of sixth-order LO phonon mode decreases.

To investigate the dependence of RRS intensity on the band gap energy, temperature dependent RRS spectra of $Zn_{0.991}Mn_{0.009}O$ is shown in figure 4(a). At 10 K, the intensity of sixth-order LO phonon mode around 3500 cm^{-1} is the largest.

However, when the temperature increases to 160 K, the seventh-order LO phonon mode around 4100 cm^{-1} becomes the largest in intensity. The behavior can be explained by considering the temperature dependence of the photoluminescence (PL). Figure 4(b) shows the PL peak position of $Zn_{0.991}Mn_{0.009}O$ as a function of the temperature, and the curve can be fitted by considering the Bose-Einstein statistical factor for phonons [33]

$$E(T) = E(0) - \frac{2a_B}{\exp(\Theta / T) - 1} \qquad (3),$$

where $E(T)$ and $E(0)$ are the energies at T K and 0 K, respectively, a_B is the strength of the electron-phonon interaction, and Θ is associated with the mean frequency of the phonons. From figure 4(a) and (b), the shift of PL position results in the LO phonon line intensity variation. To summarize, multiple LO phonon scattering in RRS spectra can be explained by using the "cascade model" [34-35], the scattered photons will have energy $\hbar\omega \cong \hbar\omega_i - n\hbar\omega_{LO}$ or $\hbar\omega \cong \hbar\omega_i - n\hbar\omega_{E_{2(high)}} - n\hbar\omega_{LO}$. Moreover, by studying RRS spectra, we find that when the scattered photon energy is close to the band gap, the LO phonon intensity will be resonantly enhanced.

Figure 5 show the low temperature (10 K) PL spectra of $Zn_{0.997}Mn_{0.003}O$ analyzed by (σ_+) and (σ_-) circular polarization at magnetic field B = 0 and B = 5 Tesla. At B = 0, no difference was observed between two circular polarization. The D^0X (at 3.356 and 3.363 eV) and RRS (at 3.306 and 3.378 eV) intensities for (σ_+)

and (σ_-) components are approximately the same. However, at B = 5 Tesla, a slight difference is observed between the two circular polarization components of the D_0X. While the intensities of the two circular polarization components of the RRS remain the same. The degree of circular polarization can be defined as

$$P = \frac{I_{\sigma+} - I_{\sigma-}}{I_{\sigma+} + I_{\sigma-}} \qquad (4),$$

where $I_{\sigma+}$ and $I_{\sigma-}$ are the intensities of the right and left circular polarization, respectively. For RRS, P = 0 at B = 0 and 5 Tesla. Whereas, for D_0X emission, P = 0 at 0 Tesla and P = 9 % at 5 Tesla. The non-zero circular polarization is due to the energy splitting of the two spin components of the D_0X, (electron -1/2 and hole -3/2) and (electron +1/2 and hole +3/2). Although, the energy separation is too small to be resolved, due the energy relaxation from the higher energy spin state to the lower energy spin state, P=9 % is observed. The dependence of circular polarization on the magnetic field shows Brillouin-type para-magnetism. No hysteresis is observed. It implies that the $Zn_{0.997}Mn_{0.003}O$ exhibits para-magnetism due sp-d exchange interaction between conduction band s electrons/valence band p electron and d electrons of the Mn atoms.

In summary, we have grown $Zn_{1-x}Mn_xO$ (x=0~0.061) thin films by PA-MBE. Transmittance measurement shows an increase of the band gap with the increasing Mn concentration. From RRS spectra, we observe LO phonon lines up to 5 and 11

order for ZnO and ZnMnO samples, respectively. From the temperature dependent RRS experiment, we find the intensities of these LO phonon lines are sensitive to the band gap position. Low temperature PL spectra of $Zn_{0.997}Mn_{0.003}O$ at magnetic field B=0 T and 5 T were investigated to calculate the degrees of circular polarization of P=0 % and 9 %, respectively.

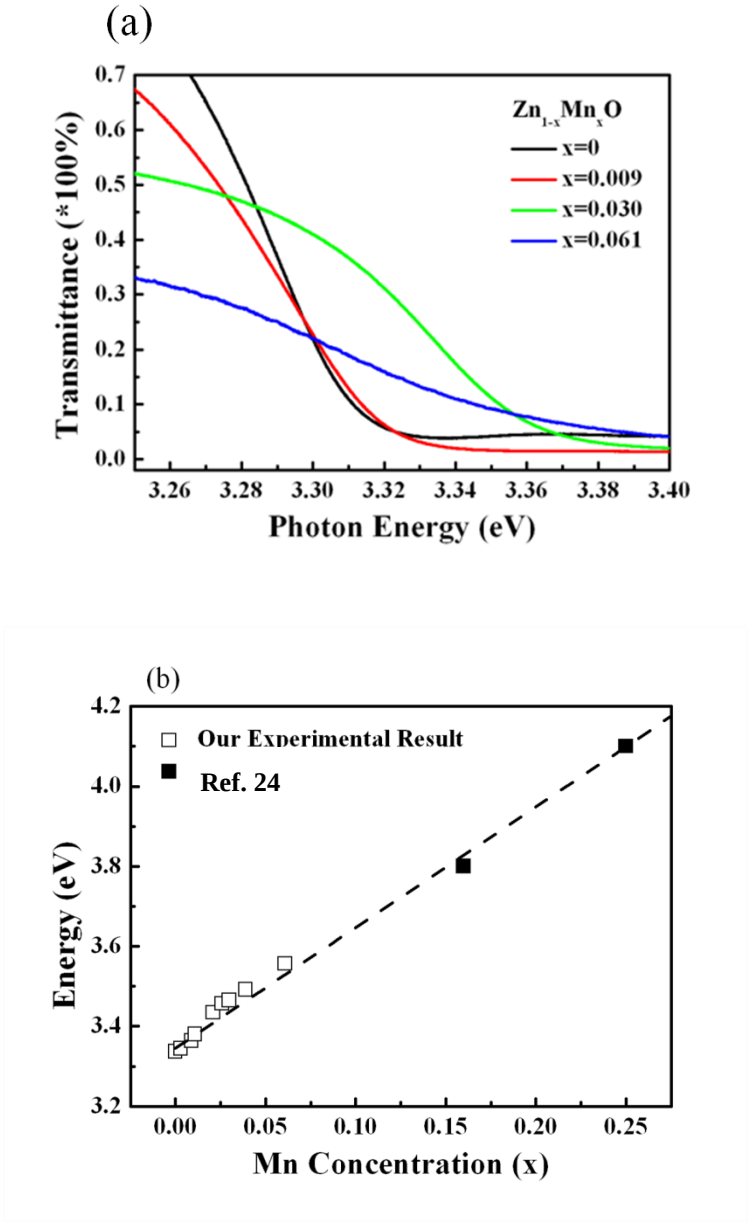

Fig.1 (a) Room temperature transmittance spectra of $Zn_{1-x}Mn_xO$ thin films with Mn concentration x=0, 0.009, 0.030 and 0.061. **(b)** The energy of absorption edge for $Zn_{1-x}Mn_xO$ thin films as a function of the Mn concentrations(x). The experimental results of ours(□) and reference 24 (■) are plotted.

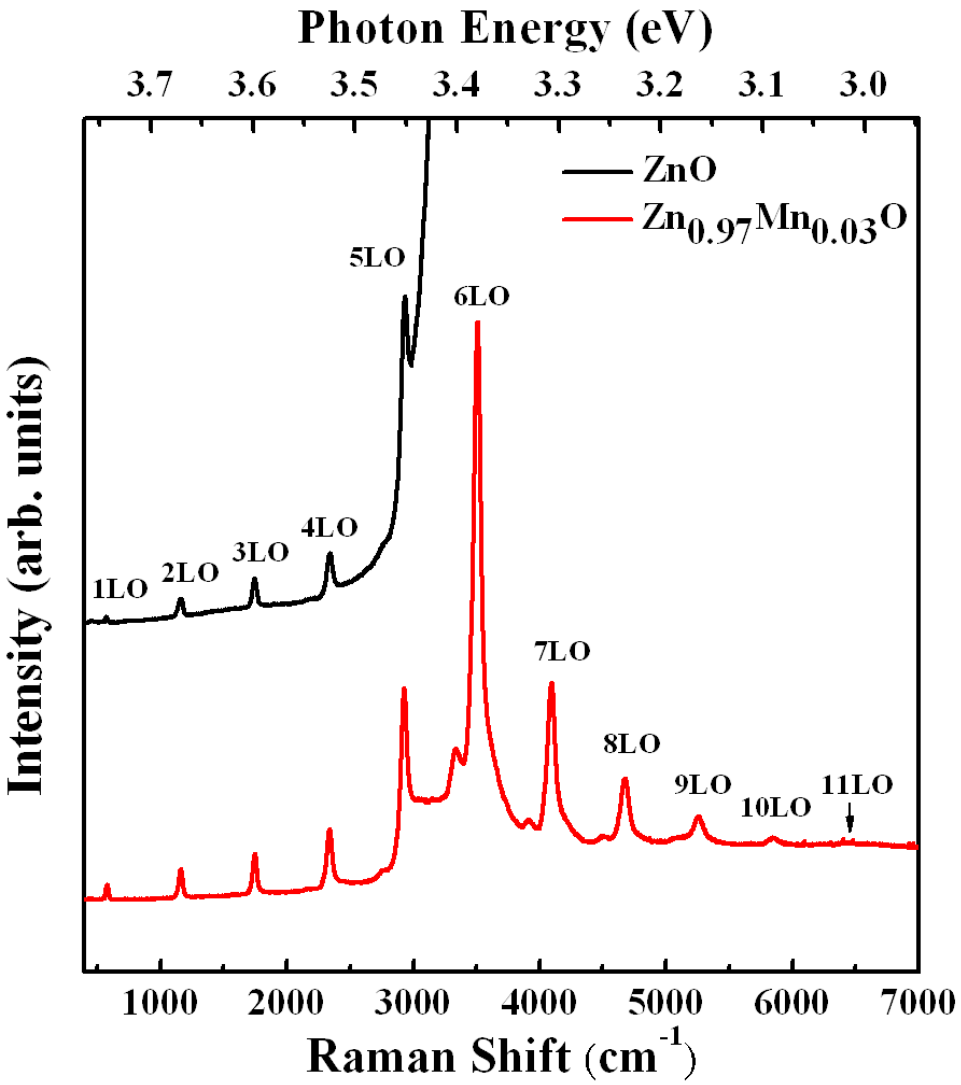

Fig. 2 Resonant Raman scatterings of ZnO and $Zn_{0.97}Mn_{0.03}O$ thin films, using the He–Cd laser (λ=325 nm).

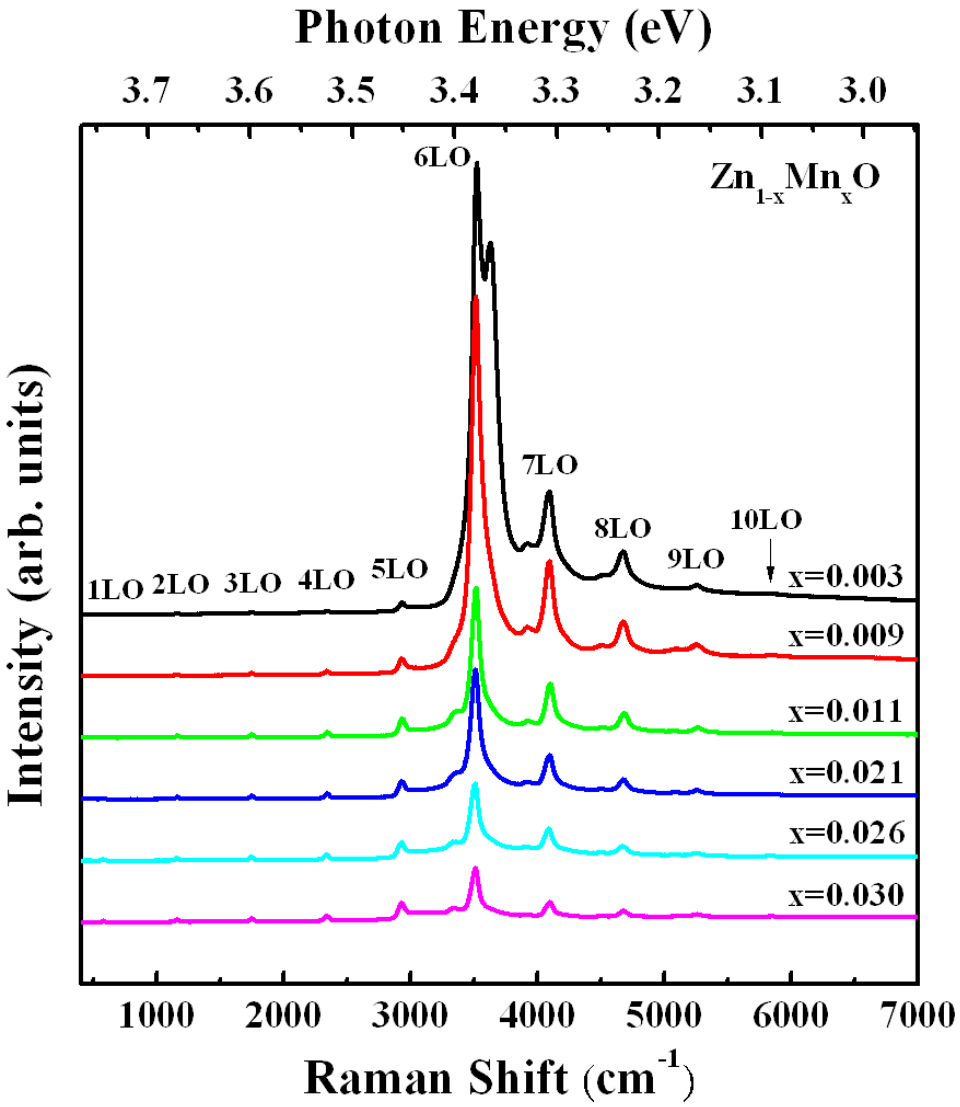

Fig. 3 Resonant Raman scatterings of $Zn_{1-x}Mn_xO$ thin films, using the He–Cd laser (λ=325 nm).

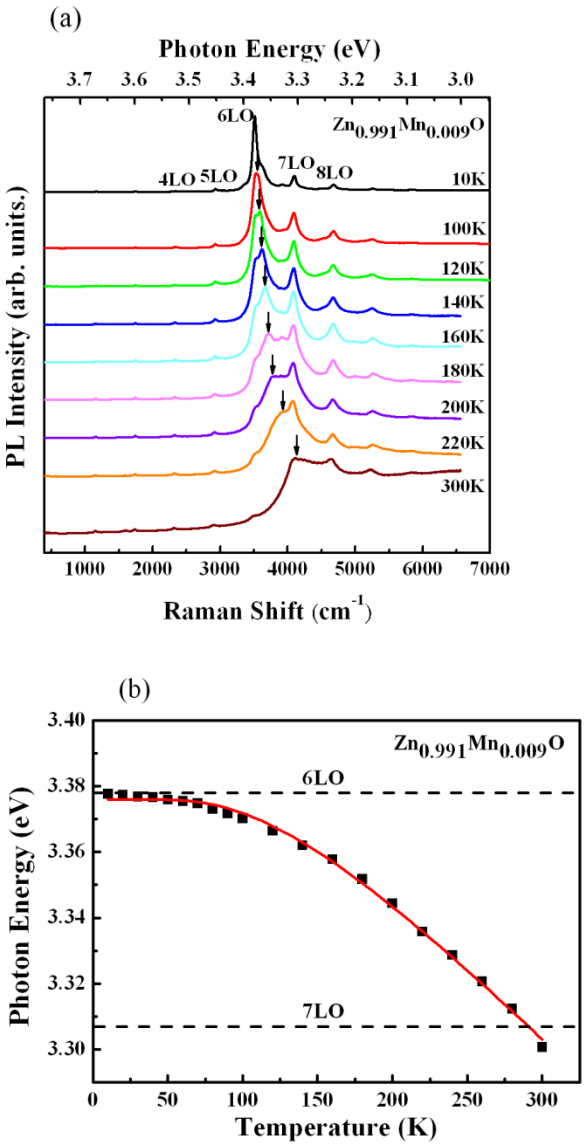

Fig. 4 (a) Resonant Raman scatterings of $Zn_{0.991}Mn_{0.009}O$ thin films with variable temperature, using the He-Cd laser (λ = 325 nm). The arrows show the PL positions. **(b)** Temperature dependent PL position of $Zn_{0.991}Mn_{0.009}O$. The solid curve describes the fit of these data by using the Bose-Einstein statistical factor for phonons. The dashed lines represents the energy positions of the scattered photons with energy $\hbar\omega \cong \hbar\omega_i - n\hbar\omega_{LO}$, n = 6 or 7.

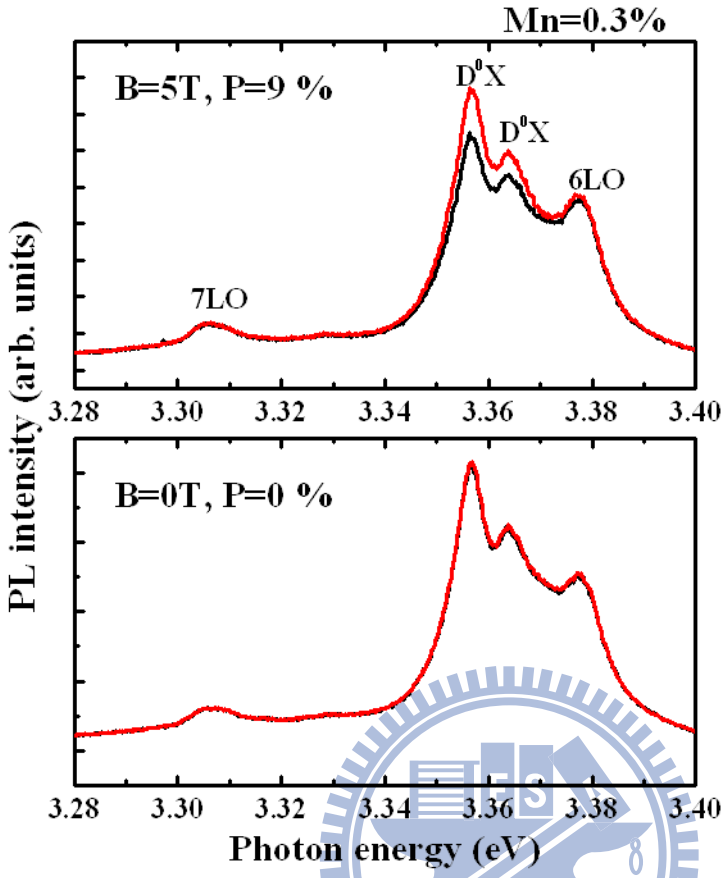

Fig. 5 Low temperature (10 K) PL spectra of $Zn_{0.997}Mn_{0.003}O$ for B = 0 and B = 5 Tesla.

Chapter 5

Thermal-activated carrier transfer in $Zn_{0.98}Cd_{0.02}O$ thin film

In this chapter, the thermal-activated carrier transfer processes in $Zn_{0.98}Cd_{0.02}O$ thin film grown by plasma-assisted molecular beam epitaxy were investigated by temperature dependent and time-resolved photoluminescence.

Fig. 1 shows the PL spectra of ZnO and $Zn_{0.98}Cd_{0.02}O$ films at 10 K. The emission peaks at 3.361 and 3.366 eV were assigned to the excitons bound to neutral donors (D_oX) [36]. The peak at 3.377 eV is attributed to the free A excitons (FX_A) [37]. When Cd atoms were introduced into ZnO, the PL band becomes broad and the spectral position of the PL peak shifts to 3.185 eV. According to the experimental results of Gruber *et al*. [38], the Cd composition herein can be estimated as 2%. Additionally, the PL emission profile of $Zn_{0.98}Cd_{0.02}O$ is not symmetry due to the existence of localized states at low energy side. The transmittance spectrum at 10 K shown in the inset shows a strong absorption near the band edge. It can be seen that the Cd incorporation reduces the band gap energy and causes a Stokes' shift of about 100 meV. The Stokes' shift is attributed to the localization of excitons due to the Cd compositional fluctuation [39]. In order to further investigate and compare the optical properties of $Zn_{0.98}Cd_{0.02}O$ with ZnO, the temperature-dependent PL measurements of

ZnO and $Zn_{0.98}Cd_{0.02}O$ were carried out. In Fig. 2 (a), both D_oX and FX_A of ZnO shift to lower energies, and the line-width broadens with increasing temperature. The PL line width broadening is related to the carrier–phonon interaction. Additionally, because of thermally activated processes of carriers, FX dominates at high temperature. In Fig. 2 (b), three PL peaks of $Zn_{0.98}Cd_{0.02}O$ labeled as P1, P2, and P3 were observed at different temperatures. The P1 emission was observed at low temperature. When T>140 K, additional peaks, P2 and P3, become visible. The intensity of P2 increases and exceeds that of P1 when T>220 K. Similar optical properties were also observed by Yang *et al*. [40] in $ZnSe_{1-x}Te_x$ (x=0.01) epilayers. In the case of $ZnSe_{1-x}Te_x$, at low temperature of 10 K, X/Te is not observed and the PL of the Te_n-bound excitons (X/Te_n) is very pronounced. The energy states of X/Te and X/Te clusters become observable as the temperature was increased. Thus, the PL peaks of P1, P2, and P3 can be attributed to the emissions from X/Cd_n, X/Cd, and X/Cd cluster, respectively. Fig. 2(c) shows the dependence of X/Cd_n intensity on temperature with a double-channels activation energy function: [41]

$$I_{PL}(T) = \frac{I_0}{1 + C_1 \exp\left(-E_{a1}/k_B T\right) + C_2 \exp\left(-E_{a2}/k_B T\right)} \quad (1).$$

Where $I_{PL}(T)$ is the integrated PL intensity at temperature T, k_B is the Boltzmann constant, Ea1 and Ea2 denote the activation energy, C is a tunneling factor, and I_0 is the integrated intensity at the low temperature limit. In this study, E_{a1}=4 meV and

E_{a2}=19 meV were extracted. The activation energy E_{a1} is attributed to the average localization energy of the X/Cd$_n$. On the other hand, the activation energy E_{a2} corresponds to thermal energy of 220 K, which is similar to the quenching temperature of X/Cd$_n$ intensity. Therefore, we consider that the activation energy E_{a2} is the energy for carriers transferred from X/Cd$_n$ to X/Cd.

In order to confirm the origin of the emissions from X/Cd, X/Cd$_n$, and X/Cd clusters, the PL peak positions of the free-exciton (FX), X/Cd, X/Cd$_n$, and X/Cd clusters as a function of temperature were plotted in Fig. 3(a). The FX peak positions obtained from transmittance are well fitted by the Vashini's prediction [42] which is written as

$$E_g(T) = E_g(0) - \alpha T^2/(\beta + T) \quad (2).$$

Where Eg(0) is the band-gap energy at T=0 K, and a and b are the corresponding thermal coefficients. The fitting is labeled by solid lines in Fig. 3(a). The X/Cd peaks exhibit a similar trend. The emission energy of X/Cd is 80 meV lower than that of FX. It implies that there is not enough energy to offer the carriers transferred from X/Cd states to FX states. Therefore, X/Cd dominates the carrier recombination at 300 K. However, the X/Cd$_n$ peak demonstrates a fast red shift at temperatures above 50 K. This phenomenon could be attributed to continuous localized states formed with the X/Cd$_n$ states. We proposed that excitons assisted by the scattering of LO phonons would transfer to the deep localized states, and the possibility of this re-localization

process is promoted as the temperature increases because the spreading of exciton wave-function enhances the interaction with LO phonon fields. In this condition, the increased temperature only causes small parts of the carriers to delocalize from the deep localized states to the shallow ones. The X/Cd_n peak redshifts dramatically until the carriers were relocalized at the X/Cd cluster states (the deepest localized states). On the contrary, as the temperature exceeds 220 K, the thermal energy overthrows the activation barrier of 19 meV, which pro- motes large amount of the carriers to escape from the deep localization and the X/Cd emission dominates. Fig. 3(b) shows the power dependent PL spectra at 220 K for $Zn_{0.98}Cd_{0.02}O$. The intensity of PL emission is enhanced with increasing excitation power. Under an excitation power of 65 W/cm^2, the emission energies of X/Cd cluster and X/Cd are at 2.782 and 3.160 eV, respectively. As the excitation power is increased, the X/Cd cluster exhibits energy blueshift and the X/Cd_n state dominates the spectrum. This result implies that the density of state for the X/Cd_n is much higher than that for the X/Cd cluster. The increasing excitation density saturates the lower energy states. As a result, the X/Cd_n state dominates the emission.

In order to provide further evidence to support the existence of localized states and to demonstrate the origin of the radiative recombination, we performed TRPL measurements at 10 K, 100 K and 150 K as shown in Fig. 4. The carrier

recombination time decreases with increasing temperature. It implies that the thermalized carriers could relax easily over along distance and find a lower local-energy minimum. Besides, the main PL peak positions undergoes no obvious energy shift over time at 10 K, reflecting the main recombination of the localized state with the same concentration of Cd. However, the main peak shifts 39 meV toward the low energy side with time at 100 K. It reveals that the thermal- activated carriers transfer to the deeper localized states via the phonon scattering. As the temperature increases to 150 K, a larger redshift of 100 meV with the delay time was found, indicating more carriers can transfer to the deeper localized states. In combination with temperature-dependent PL and TRPL, we demonstrate the carrier transfer dynamics in $Zn_{0.98}Cd_{0.02}O$. The strong redshift of the X/Cd_n peak energy is caused by the carrier transfers to the deep localized states as T<220 K. Moreover, a delocalization process occurs as the temperature exceeds 220K.

In summary, emissions of X/Cd, X/Cd_n, and X/Cd cluster from $Zn_{0.98}Cd_{0.02}O$ thin film were investigated by PL and TRPL spectroscopy. Two emission peaks, which are attributed to the carrier recombinations of X/Cd states and X/Cd cluster states, were observed at elevated temperatures. From 50 to 220 K, the carriers transfer from shallow X/Cd_n states to deep localized X/Cd_n states. Above 220 K, the carriers escape from the deep localized X/Cd_n states to X/Cd states.

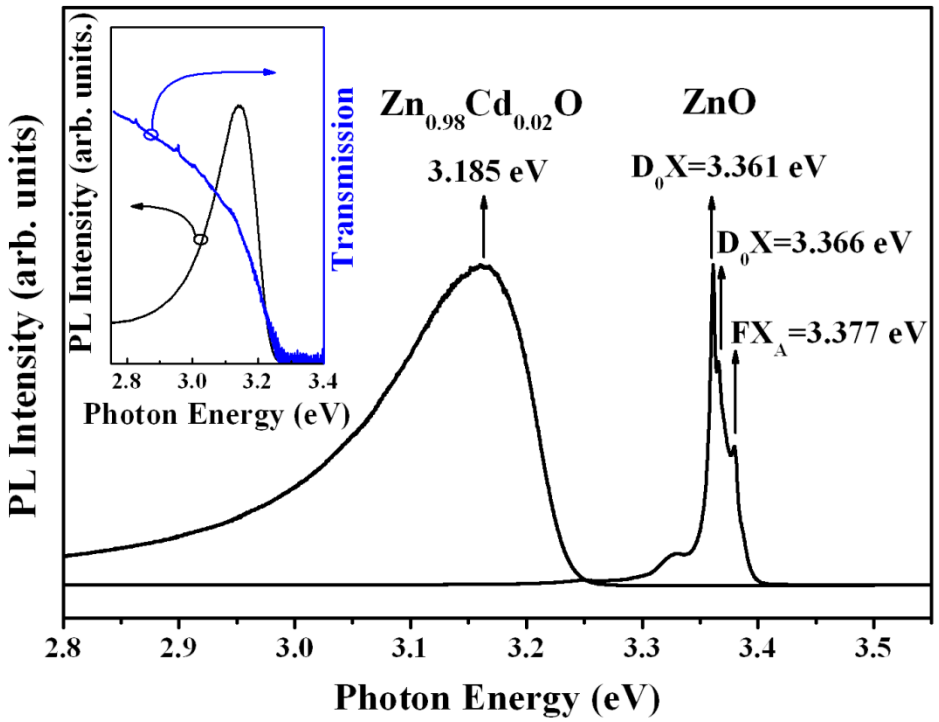

Fig. 1 PL spectra of ZnO and $Zn_{0.98}Cd_{0.02}O$ films at10 K. The inset shows the PL and transmittance spectra of $Zn_{0.98}Cd_{0.02}O$ at 10 K.

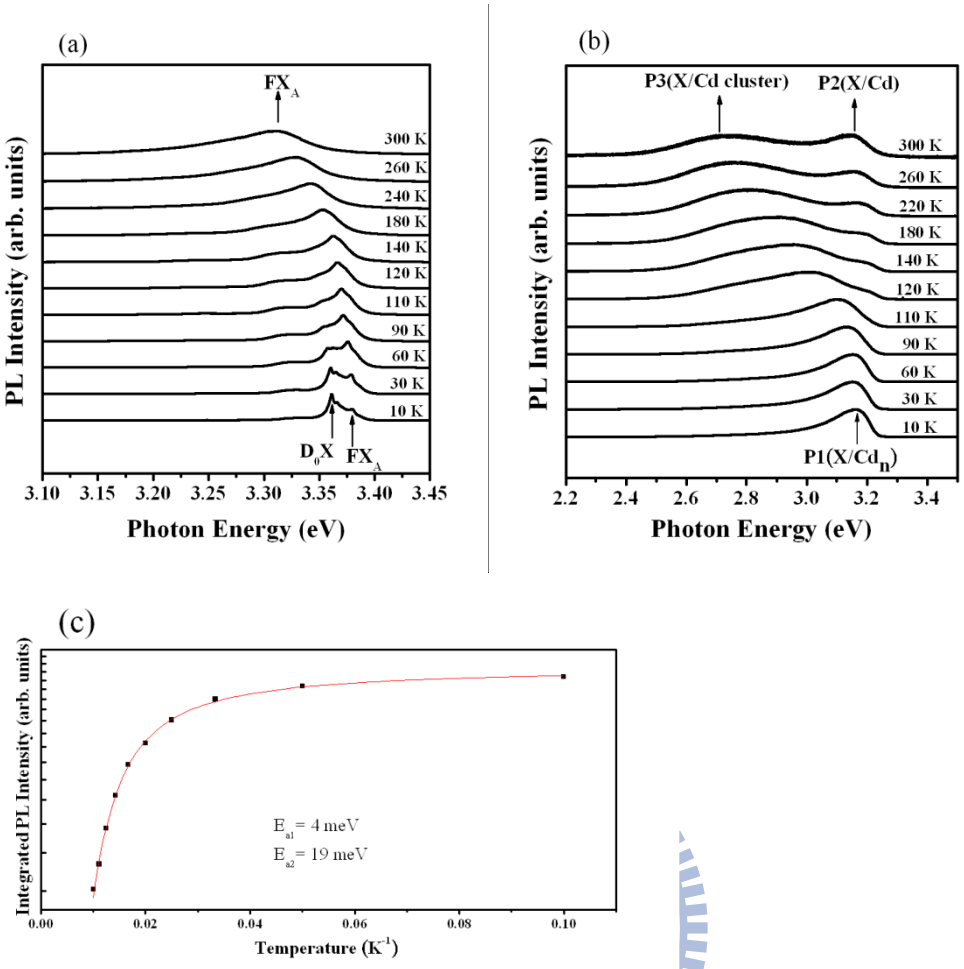

Fig. 2 PL spectra of **(a)** ZnO and **(b)** $Zn_{0.98}Cd_{0.02}O$ thin films at various temperatures. **(c)** Integrated PL intensity of X/Cd_n as a function of temperature for $Zn_{0.98}Cd_{0.02}O$. The solid line is fitted by Eq. (1).

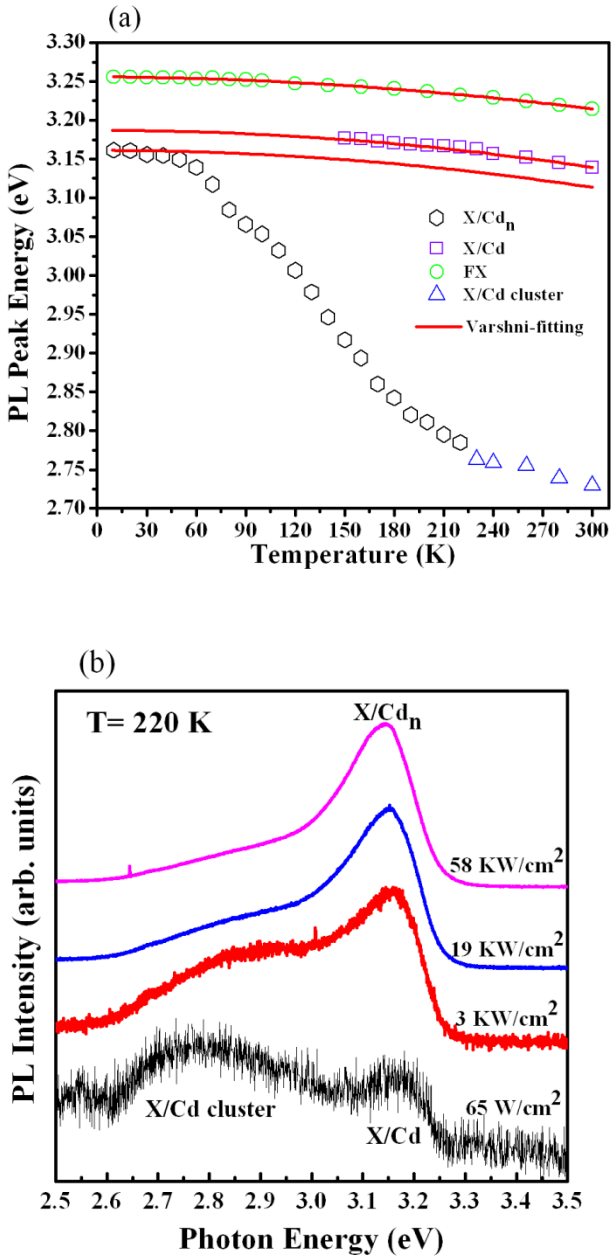

Fig. 3 (a) PL peak energy trace of X/Cd, X/Cd$_n$, X/Cd cluster and FX at various temperatures. The solid lines are Varshni's fits. (b) Power dependent spectra of $Zn_{0.98}Cd_{0.02}O$ at 220 K.

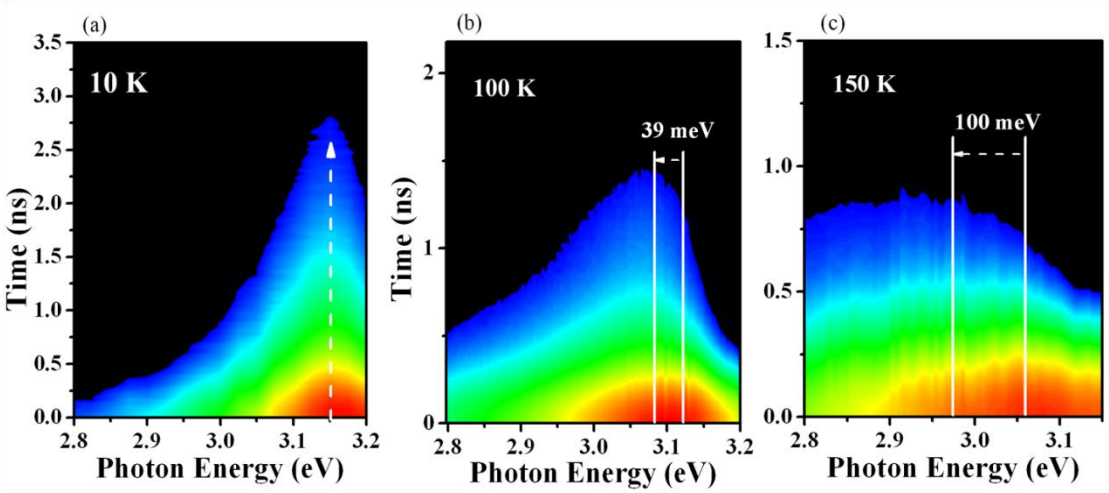

Fig. 4 Temporal evolution of the PL spectra at **(a)** 10 K, **(b)** 100 K, and **(c)** 150 K.

Chapter 6

Growth and carrier dynamics of $Zn_{1-x}Cd_xO$ thin films with visible light emission

In previous chapter, the recombination dynamics of $Zn_{1-x}Cd_xO$ thin films with low Cd concentration (x=0.02) sample has been studied. For high efficient light emitting device application or solar cell application, the growth and optical studies of high quality $Zn_{1-x}Cd_xO$ with high Cd concentration are demanded.

In this chapter, high Cd concentration of $Zn_{1-x}Cd_xO$ was controlled by adjusting the Cd/Zn beam pressure ratio. The Cd content in $Zn_{1-x}Cd_xO$ was determined by energy dispersive x-ray spectroscopy and showed concentrations ranged from 0.062 to 0.497 in Fig. 1. The Cd content, x, increases linearly with increasing beam equivalent pressure, which was measured by a nude ionization gauge placed in front of the substrate. It is the first time that $Zn_{1-x}Cd_xO$ thin film grown at 350℃ with Cd composition up to 49.7 % by PA-MBE. During the growth of $Zn_{0.503}Cd_{0.497}O$ thin film, a streaky RHEED pattern was observed along the (11-2) azimuth, as shown in the inset of Fig. 1. It implies that $Zn_{0.503}Cd_{0.497}O$ thin film has smooth surface.

Figure 2(a) shows the PL spectra of $Zn_{1-x}Cd_xO$ films taken at 10 K. By

increasing *x*, the luminescence peak shifted to a lower energy from 3.36 eV of ZnO to 1.91 eV of $Zn_{0.503}Cd_{0.497}O$. It is difficult to grow $Zn_{1-x}Cd_xO$ with high Cd content. Because, ZnO and CdO have different crystal structure and the growth temperatures are very different [43]. Furthermore, there is a large lattice mismatch between ZnO and CdO. It is the first time that high quality $Zn_{1-x}Cd_xO$ thin film can be grown at 350℃ with red PL peak emission by PA-MBE. Figure 2(b) shows the measured and referred values of PL peak position versus Cd content *x*. The solid line,

$$E_{PL} = -1.05x + 3.35\,(\text{eV}) \qquad (1),$$

connects the band gaps of the two binary compounds, ZnO (3.35 eV) and CdO (2.20 eV) [43].

The red dashed line,

$$E_{PL} = 3.36 - 6.12x + 6.43x^2\,(\text{eV}) \qquad (2),$$

describes our experimental data for the PL emission peaks. For comparison, the PL results summarized from previous reports [38,44-45], can be illustrated by the dotted line of the following equation,

$$E_{PL} = 3.35 - 9.19x + 8.14x^2\,(\text{eV}) \qquad (3).$$

The deviation from the solid line, band bowing, is due the composition fluctuation (chemical disorder), which creates local potential well to lower the emission energy. The band bowing of the previous reports is more pronounced than ours. It implies our

samples have better crystal quality with less chemical disorder.

In order to further investigate the optical properties of $Zn_{1-x}Cd_xO$ to study the band bowing effect, temperature-dependent PL measurements of $Zn_{1-x}Cd_xO$ with x= 0.062, 0.185, 0.366 and 0.454 were carried out. In Fig. 3, the near band edge emission of $Zn_{0.938}Cd_{0.062}O$ simply shifts to lower energy and the line-width broadens with increasing temperature. However, the PL peak position of $Zn_{0.815}Cd_{0.185}O$ shows abnormal red-blue-red shift with increasing temperature. A red shift is observed at temperature below 90 K. As the temperature is increased above 90K, the PL peak position shifts to higher energy first, then moves towards lower energy as the temperature is increased above 120K. In the case of $Zn_{0.634}Cd_{0.366}O$ and $Zn_{0.546}Cd_{0.454}O$, the dependence of peak position on temperature shows initial red-shift and then blue-shift as large as several tenth meV. These novel temperature behaviors of PL emission peak are attributed to the existence of complex localized states, X/Cdn and X/Cd clusters, as described in previous chapter. For $Zn_{0.815}Cd_{0.185}O$, due to insufficient thermal energy for localized carriers to overcome the localization potential at low temperature, they relax to the lower-lying localized states prior to recombination. As the temperature increases localized carriers are thermalized, occupy higher energy states and leads to blue shift in emission peak. At temperature above 120 K the red shift due to temperature induced band gap shrinkage dominates

over the blue shift. The PL peak position of $Zn_{0.634}Cd_{0.366}O$ and $Zn_{0.546}Cd_{0.454}O$ demonstrates red-blue (V-shaped) shift with increasing temperature. The red shift observed at temperature below 100 K and 120 K respectively, and then the blue shift behavior is observed. Similar optical trends were also observed by Lin *et al.* in $ZnSe_{1-x}Te_x$ (x=0.05) epilayers [46]. In the case of $ZnSe_{0.095}Te_{0.05}$, the V-shaped energy shift over the same range of temperatures (10–300 K) are ascribed a rather deep localization. Additionally, the Stokes' shift of $Zn_{0.634}Cd_{0.366}O$ and $Zn_{0.546}Cd_{0.454}O$ shown in Fig. 2(b) is as large as 1 eV. Thus, V-shaped energy shift of $Zn_{0.634}Cd_{0.366}O$ and $Zn_{0.546}Cd_{0.454}O$ indicates that the carriers are still localized in localized states at room temperature.

The PL peak positions of $Zn_{0.938}Cd_{0.062}O$, $Zn_{0.815}Cd_{0.185}O$, and $Zn_{0.634}Cd_{0.366}O$, as a function of temperature were plotted in figure 4(a). The PL peak positions of $Zn_{0.938}Cd_{0.062}O$ are well fitted by the Vashini's prediction which is written as $E_g(T) = E_g(0) - \alpha T^2/(\beta + T)$ [42], where $E_g(0)$ is the band-gap energy at T=0 K, and α and β are the corresponding thermal coefficients. The fitting is labeled by dashed lines in Fig. 4(a). However, the Vashini's trends don't completely agree the trends of the PL peak positions in $Zn_{0.815}Cd_{0.185}O$ and $Zn_{0.634}Cd_{0.366}O$ as a function of temperature. It implies the existence of carrier transfer between localized states. In previous report, the cathode-luminescence results also showed that there are clusters

in $Zn_{1-x}Cd_xO$ crystal with high Cd concentration [47]. Similar localized states were also observed by Yang *et al.*in $ZnSe_{1-x}Te_x$ epilayers., the localized states of $ZnSe_{1-x}Te_x$ include the Te_n bound exciton and the Te_n clusters bound exciton [40]. Therefore, the PL emission of $Zn_{0.815}Cd_{0.185}O$ and $Zn_{0.634}Cd_{0.366}O$ can be attributed to the emissions from the Cd_n bound exciton and the Cd_n clusters bound exciton, respectively. The Cd_n bound exciton has been identified here as the exciton bound to two or more isolated Cd. Thus, the localized states with different localized energy were caused the Cd_n bound exciton. On the other hand, the Cd_n clusters bound exciton has been identified here as the exciton bound to the deepest localized states. Fig. 4(b) shows the temperature dependence of the integrated PL intensity for $Zn_{0.938}Cd_{0.062}O$, $Zn_{0.815}Cd_{0.185}O$, and $Zn_{0.634}Cd_{0.366}O$. The integrated PL intensity shows a typical behavior for thermally activated nonradiative recombinations of $Zn_{0.938}Cd_{0.062}O$. The integrated PL intensity of the $Zn_{0.815}Cd_{0.185}O$ with increasing temperature first decreases fast below 40 K, then slows down between 40 and 60 K, and finally decreases quickly again for *T* higher than 60 K. On the contrary, the integrated PL intensity of the $Zn_{0.634}Cd_{0.366}O$ with increasing temperature first decreases below 150 K, then increases above 150 K. Similar optical properties were also observed in quantum dots system [48]. As a result, thermally activated transfer of carriers was in the quantum dots with different localized states. Thus, the phenomenon of the

integrated PL intensity in $Zn_{0.634}Cd_{0.366}O$ can be attributed to the carrier transition from Cd_n clusters to Cd_n bound exciton. Fig. 4(c) shows the dependence of the integrated PL intensity in $Zn_{0.634}Cd_{0.366}O$ on temperature with an activation energy function: [41]

$$I_{PL}(T) = \frac{I_0}{1 + C\exp\left(-E_a / k_B T\right)} \quad (4),$$

where $I_{PL}(T)$ is the integrated PL intensity at temperature T, k_B is the Boltzmann constant, E_a denotes the activation energy, C is a tunneling factor, and I_0 is the integrated intensity at the low temperature limit. In this study, E_a=15 meV was extracted. The activation energy E_a corresponds to thermal energy around 150 K, which is similar to the temperature that PL peak positions start to blue shift and integrated PL intensity increases. When the temperature exceeds 150 K, the PL quenching of Cd_n clusters bound exciton and the PL increasing of Cd_n bound exciton becomes dominant.

In summary, this study investigated the growth and carrier dynamics of $Zn_{1-x}Cd_xO$. High quality $Zn_{1-x}Cd_xO$ thin films with visible light emission were grown on sapphire substrates by PA-MBE. The maximum concentration of Cd is 49.7 % which can be systematically adjusted via the Cd/Zn beam pressure ratio. The S-shaped dependence of the PL peak positions indicates that Cd_n bound exciton lead the different localized states in alloying. The V-shaped dependence of the PL peak

energy in high Cd concentration $Zn_{1-x}Cd_xO$ indicates that Cd_n clusters bound exciton, in which the carriers are deeply trapped below 150 K. Above 150 K, the carriers can escape from the deepest localized Cd_n clusters states to shallow localized Cd_n states. An activation energy E*a*=15 meV was observed for $Zn_{0.634}Cd_{0.366}O$, and the corresponding thermal energy around 150 K, coincides the temperature where the blue shift starts and integrated PL intensity increases.

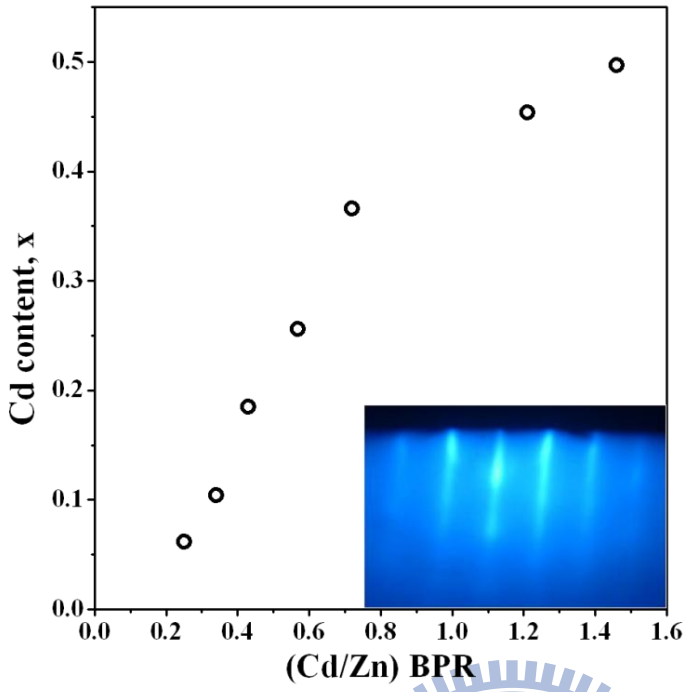

Fig. 1 Cd content increases linearly with the increasing Cd/Zn beam pressure ratio. The inset shows the RHEED pattern of $Zn_{0.503}Cd_{0.497}O$ taken along the (11-2) azimuth.

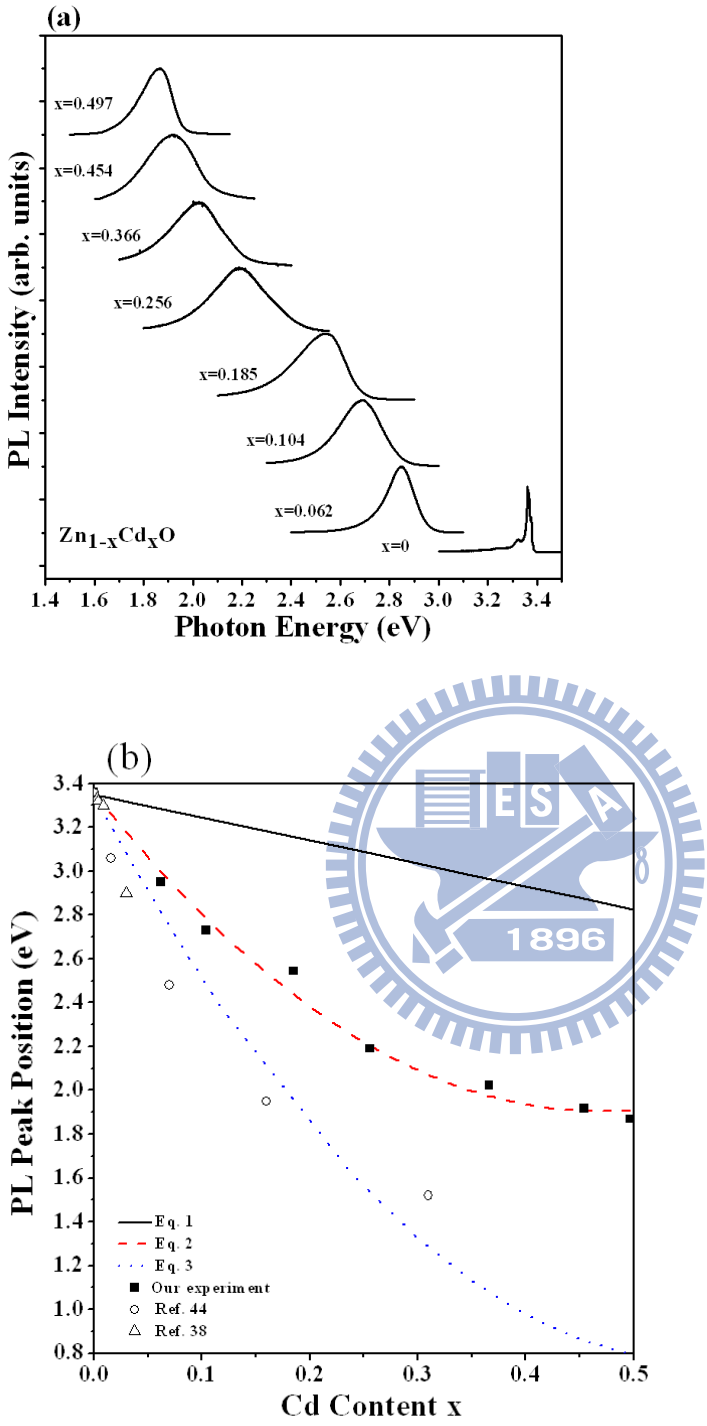

Fig. 2 (a) PL spectra of the $Zn_{1-x}Cd_xO$ films ($0 \leqq x \leqq 0.497$) at 10 K. **(b)** PL peak energy of $Zn_{1-x}Cd_xO$ as a function of Cd content *x*.

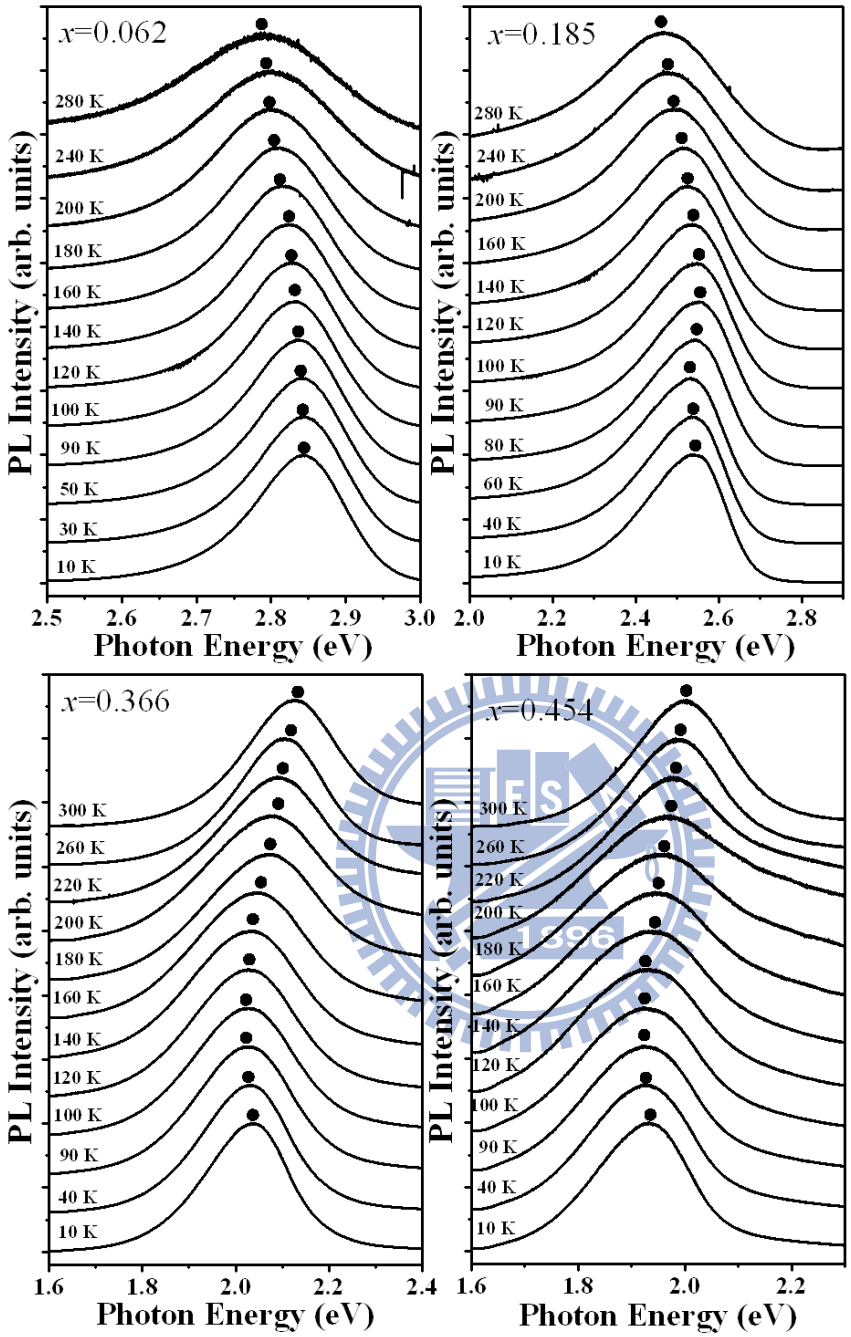

Fig. 3 PL spectra of $Zn_{1-x}Cd_xO$ with x= 0.062, 0.185, 0.366 and 0.454 at various temperatures.

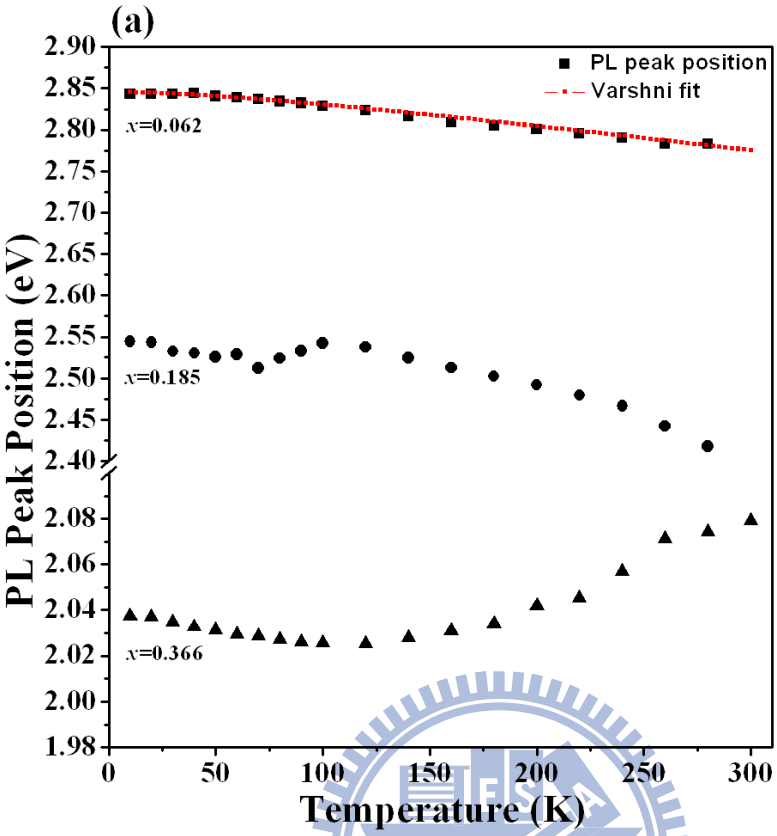
(a)
PL peak position
Varshni fit
x=0.062
x=0.185
x=0.366
PL Peak Position (eV)
Temperature (K)

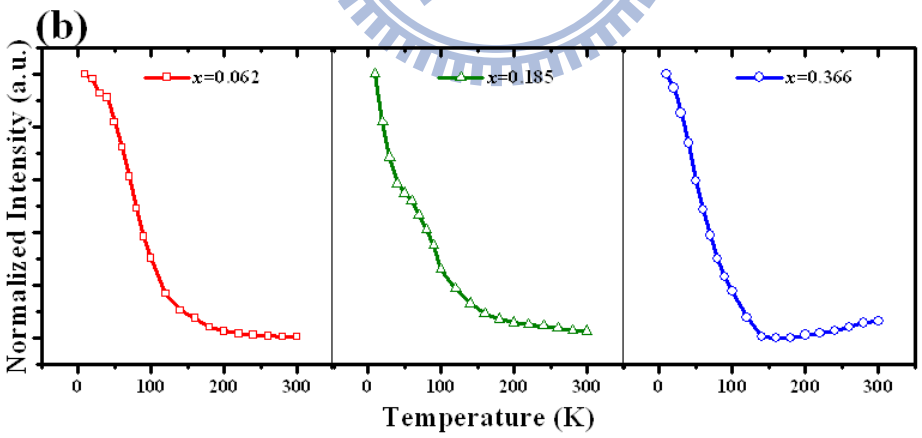
(b)
x=0.062
x=0.185
x=0.366
Normalized Intensity (a.u.)
Temperature (K)

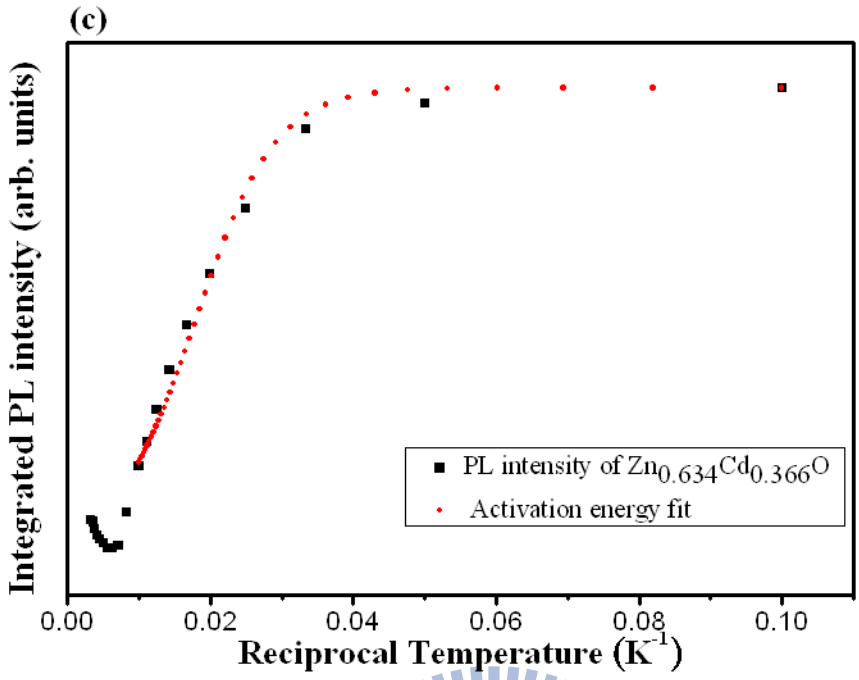

Fig. 4 (a) PL peak energy of $Zn_{0.938}Cd_{0.062}O$, $Zn_{0.815}Cd_{0.185}O$, and $Zn_{0.634}Cd_{0.366}O$ at various temperatures. The dotted line is the Varshni's fit. **(b)** Integrated PL intensity as a function of temperature for $Zn_{0.938}Cd_{0.062}O$, $Zn_{0.815}Cd_{0.185}O$, and $Zn_{0.634}Cd_{0.366}O$. **(c)** Integrated PL intensity as a function of temperature for the $Zn_{0.634}Cd_{0.366}O$. The dotted line is fitted by Eq. (4).

Chapter 7

Optical properties of the graded $Zn_{1-x}Cd_xO$ film

In previous chapters, growth and optical properties of $Zn_{1-x}Cd_xO$ thin films with x=0~0.497 were discussed. In this chapter, PL, transmittance, and TRPL spectroscopy techniques will be employed to study the recombination processes in graded band-gap $Zn_{1-x}Cd_xO$ (x=0~25.9%) multilayers for possible applications in photonic devices.

The sample comprising 4-layers with variable Cd-content was grown on c-sapphire by PA-MBE. The energy band diagram and the arrangement of the graded layers are presented in Fig. 1(a). Fig. 1(b) shows the PL spectrum of the graded $Zn_{1-x}Cd_xO$ film at 10 K. The emission peak at 3.36 eV is assigned to the excitons bound to neutral donors (D_oX) from ZnO. The region of the broad band emission is from 1.40 eV to 3.2 eV. We propose that the broad band emission exhibit the near-band edge (NBE) emission and localized states emission of $Zn_{1-x}Cd_xO$.

Fig. 2(a) presents the broad band emission from 1.40 eV to 3.2 eV. The dotted-lines in Fig. 2(a) are the curve fitting of the peak. One dotted line with peak energy at 2.96eV is due to the NBE emission, and the others are associated with the emissions of the localized states for the graded $Zn_{1-x}Cd_xO$. The peak energies of the localized-state-emissions are 2.61 eV (x=14.7%), 2.43 eV (x =19.2%), and 2.22 eV (x

=25.9%). In order to confirm the assignments for NBE emission of graded $Zn_{1-x}Cd_xO$, we performed the transmittance spectrum measurement at 10 K as shown in Fig. 2(b). In combination with PL spectrum, two NBE emissions from the ZnO and graded $Zn_{1-x}Cd_xO$ are observed. Therefore, it indicates that the broad band emission from 2.80 eV to 3.20 eV is due to the NBE emission from the graded $Zn_{1-x}Cd_xO$.

Fig. 3(a) shows the PL spectra of the graded $Zn_{1-x}Cd_xO$ and the $Zn_{0.741}Cd_{0.259}O$ at10 K. The PL peak energy of $Zn_{0.741}Cd_{0.259}O$ is 2.17 eV, which is close to the peak energy of the graded $Zn_{1-x}Cd_xO$ with x=0.259. This verify the broad band emission from 1.40 eV to 2.80 eV is attributed to the localized-state emissions of the graded $Zn_{1-x}Cd_xO$. The inset shows the PL spectra with log scale. A weak broad band emission of the graded $Zn_{1-x}Cd_xO$ from 2.80 eV to 3.20 eV was clearly observed. The broad band emission from the graded $Zn_{1-x}Cd_xO$ film overlaps with the NBE emission from the $Zn_{0.741}Cd_{0.259}O$. In addition, Fig. 3(b) shows the transmittance spectra of the graded $Zn_{1-x}Cd_xO$ and the $Zn_{0.741}Cd_{0.259}O$ taken at 10 K. The transmittance spectra confirm the results of PL. Fig. 3(c) shows PL spectra taken at 10 K from the graded $Zn_{1-x}Cd_xO$ using 325 nm and 377 nm excitation. Because the 377 nm excitation is near the band gap of graded $Zn_{1-x}Cd_xO$, the resonant excitation results in stronger and well resolved NBE emission. The NBE emission includes three recombinations at 3.11 eV, 3.01 eV, and 2.87 eV, which correspond to the localized-state-emissions at

2.61 eV(Cd=14.7%), 2.43 eV(Cd=19.2%), and 2.22 eV(Cd=25.9%), respectively. Hence, these results verify again that the broad band emission from 2.80 eV to 3.20 eV is due to the NBE emission of the graded $Zn_{1-x}Cd_xO$. To our knowledge, there is no report on the observation of NBE emission from $Zn_{1-x}Cd_xO$ with high Cd concentration due to the existence of strong localized-state-emissions. Additionally, the PL emission of the $Zn_{1-x}Cd_xO$ covers red light, green light, and blue light. As a result, the white PL emission can be observed by naked eye. The white PL emission of the graded $Zn_{1-x}Cd_xO$ film was shown in Fig. 3(d).

In order to understand the carrier recombination dynamics of the graded $Zn_{1-x}Cd_xO$, the temperature-dependent PL measurement of the graded $Zn_{1-x}Cd_xO$ was carried out. In Fig. 4, the line-width of the graded $Zn_{1-x}Cd_xO$ broadens with increasing temperature, but the PL intensity of the graded $Zn_{1-x}Cd_xO$ with increasing temperature first decreases below 200 K, then increases above 200 K. Similar optical trends were also observed in our previous report of $Zn_{1-x}Cd_xO$ thin film with high Cd concentration. This phenomenon was attributed to the carrier transition from deep localized state to the shallow localized state. The integrated PL intensity of the graded $Zn_{1-x}Cd_xO$ as a function of temperature was plotted in the inset of Fig. 4. By using the integrated PL intensity at 10 K as a reference, the intensity ratio of the high temperature PL to 10K PL can be regarded as the internal quantum efficiency (IQE)

[49-50]. The integrated PL intensity in a low temperature range is higher than that at 10 K. This behavior is due to the flow of carriers, which are photo-excited in the ZnO buffer layer, into the graded $Zn_{1-x}Cd_xO$ layers for PL emission. The IQE read at our sample is 33.67 %. The IQE of our sample is higher than other recently reports about $Zn_{1-x}Cd_xO$ [51-52].

TRPL measurements were detected at 3.11 eV and revealed multi-exponential nature of the recombination processes in graded $Zn_{1-x}Cd_xO$. Typical PL decay profiles at different temperatures are illustrated in Fig. 5(a). The PL decay profiles reveal non-single-exponential decay and can be decomposed into a fast (initial) and a slow (tail) component. As the temperature is increased above 60 K, the PL decay time of the slow component will increase gradually. This phenomenon becomes obviously when the temperature is increased above 140 K. None of the TRPL spectra could be fitted by a mono-exponential decay. These experimental profiles indicate complex decay dynamics in graded $Zn_{1-x}Cd_xO$. To make a more quantitative analysis of the decay behavior, the decay curves are fitted by the stretched exponential function [53],

$$I(t) = I_0 \cdot e^{-(t/\tau)^{\beta}}, \quad (1)$$

where β is the stretching exponent and τ is the exciton lifetime. Fig. 5(b) displays the measured τ and β as a function of temperature. There are two steps in the temperature dependent PL decay time, τ. β show the similar temperature dependence and the steps

occur at the same temperature as τ. This phenomenon indicates initial transfer of carriers from the deep localized state to the shallow localized state. The carrier transferring phenomena occurs at about 60 and 140 K (as the arrow line). The β decreases at 60 and 140K. On the contrary, τ increases at the same temperatures.

The measured PL decay parameters reflect several competing recombination processes. The radiative and non-radiative lifetimes can be extracted from the measured PL decay parameters by the following equation [54-56],

$$\frac{1}{\tau_{PL}(T)} = \frac{1}{\tau_R(T)} + \frac{1}{\tau_{NR}(T)}, \quad (2)$$

$$\eta_{\text{int}}(T) = \frac{1}{1+\tau_R(T)/\tau_{NR}(T)}, \quad (3)$$

$$\eta_{\text{int}}(T) = I_{PL}(T)/I_0\ , \quad (4)$$

$$\tau_{NR}(T) = \frac{\tau_{PL}(T)}{1-\eta_{\text{int}}(T)},\ \ \tau_R(T) = \frac{\tau_{PL}(T)}{\eta_{\text{int}}(T)}, \quad (5)$$

where τ_{PL} is the measured PL decay time, τ_R and τ_{NR} are correspondingly radiative and non-radiative lifetimes, and η_{int} stands for the IQE. Fig. 5(c) illustrates the above procedure and shows the extracted radiative and nonradiative lifetime parameters. Here, we introduce an auxiliary parameter, transition temperature T_{TR}, which allows a qualitative description of the competition between radiative and non-radiative recombination processes in graded $Zn_{1-x}Cd_xO$. Although the non-radiative recombination gradually dominated the τ_{PL} after 120 K, the gap between radiative and non-radiative recombination reaches balance above 180 K. Therefore, it indicates that the PL intensity increases at high temperature.

In summary, the origin of radiative recombination and dynamics of the charge carriers in the graded $Zn_{1-x}Cd_xO$ multilayers was investigated by PL and TRPL spectroscopy. We confirmed that the broad band emission exhibited the NBE emission and localized states emission of $Zn_{1-x}Cd_xO$. The high IQE of 33.67 % was achieved. Strong evidence of exciton transfer from the deep localized state to the shallow localized state was observed. In addition, the radiative and non-radiative recombination arrive balance at high temperature. This result corroborates with the phenomena that the PL intensity increases at high temperature. The high IQE of $Zn_{1-x}Cd_xO$ proposes this material has potential application in high efficiency photonic devices.

(a)

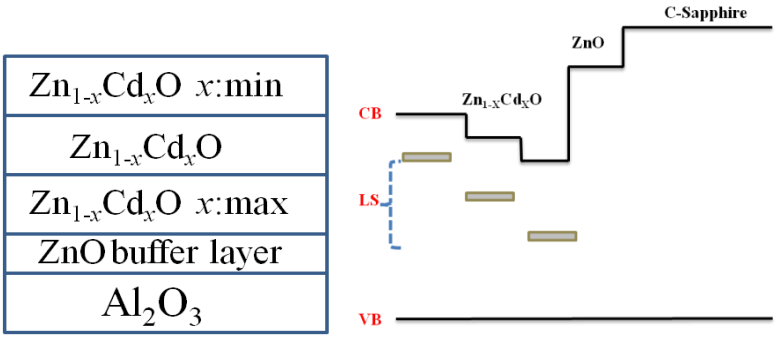

(b)

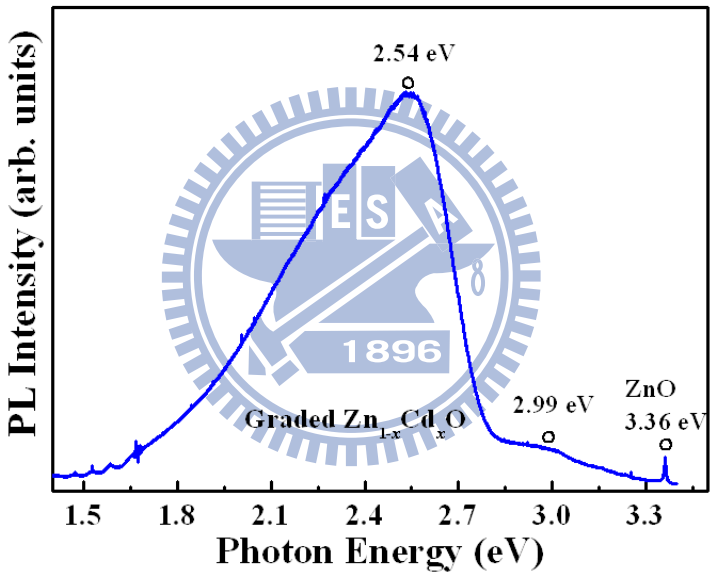

Fig.1 (a) Growth profile of $Zn_{1-x}Cd_xO$ structures and schematic graded band gap diagram. **(b)** PL spectra of the graded $Zn_{1-x}Cd_xO$ film at 10 K.

(a)

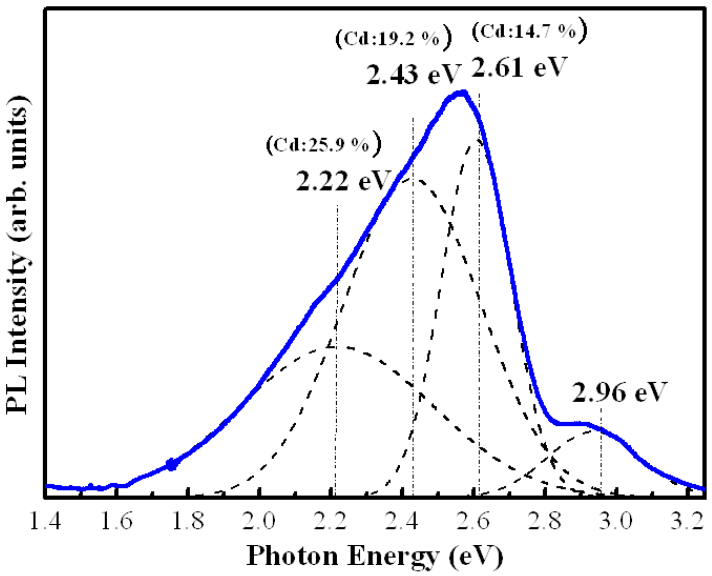

(b)

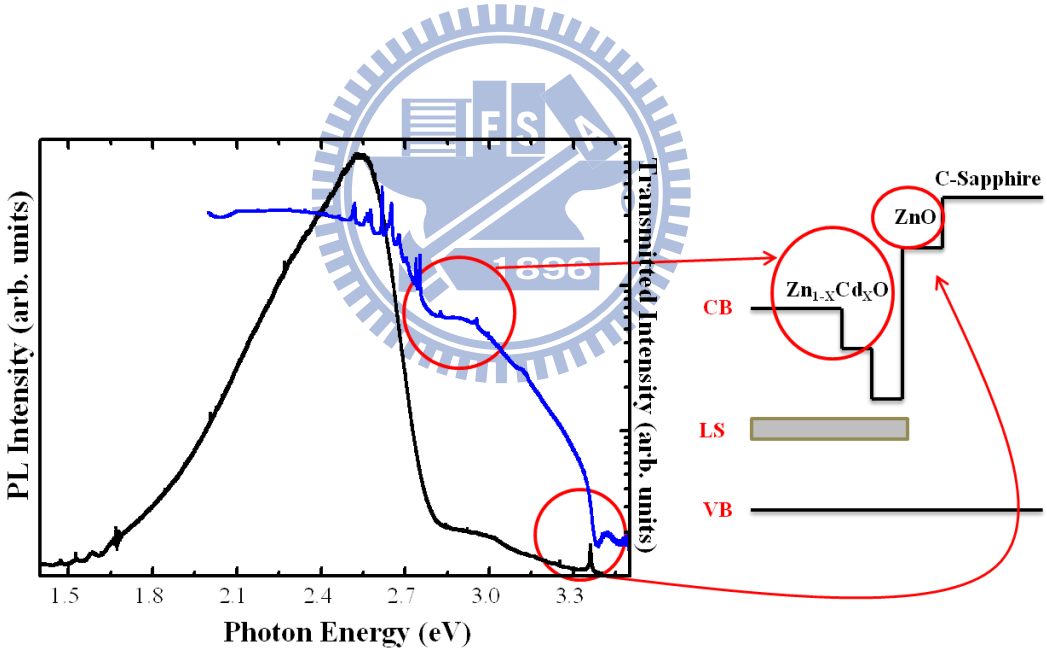

Fig. 2 (a) PL spectra of the graded $Zn_{1-x}Cd_xO$ film at10 K. The spectrum range is from 1.40 eV to 3.2 eV and the dotted-lines were curve fitting to the spectrum. **(b)** PL and transmittance spectra of the graded $Zn_{1-x}Cd_xO$ film at 10 K.

(a)

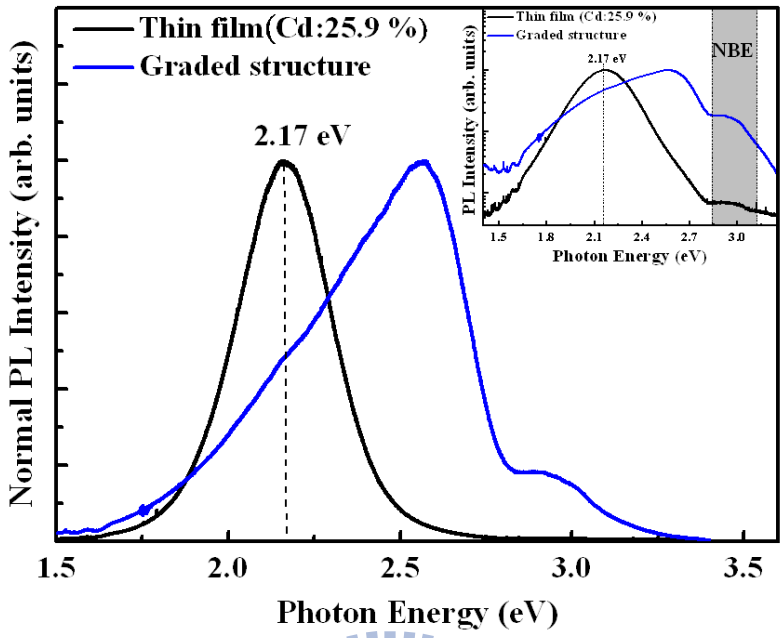
Thin film(Cd:25.9 %)
Graded structure
2.17 eV
Normal PL Intensity (arb. units)
Photon Energy (eV)
1.5
2.0
2.5
3.0
3.5
Thin film (Cd:25.9 %)
Graded structure
2.17 eV
NBE
PL Intensity (arb. units)
Photon Energy (eV)
1.5
1.8
2.1
2.4
2.7
3.0

(b)

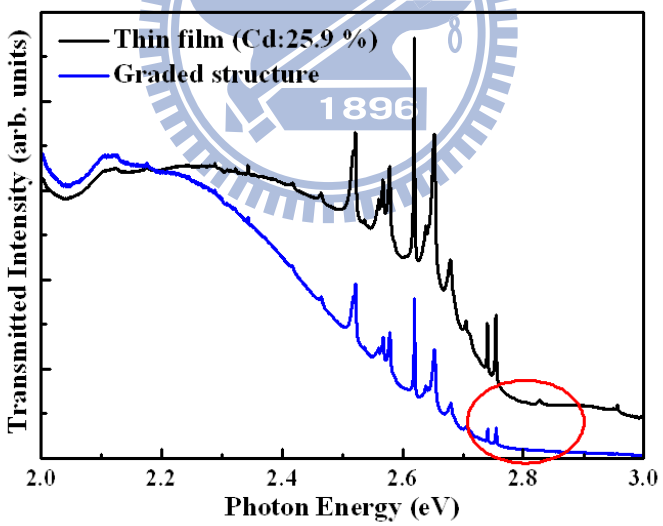
Thin film (Cd:25.9 %)
Graded structure
Transmitted Intensity (arb. units)
Photon Energy (eV)
2.0
2.2
2.4
2.6
2.8
3.0

(c)

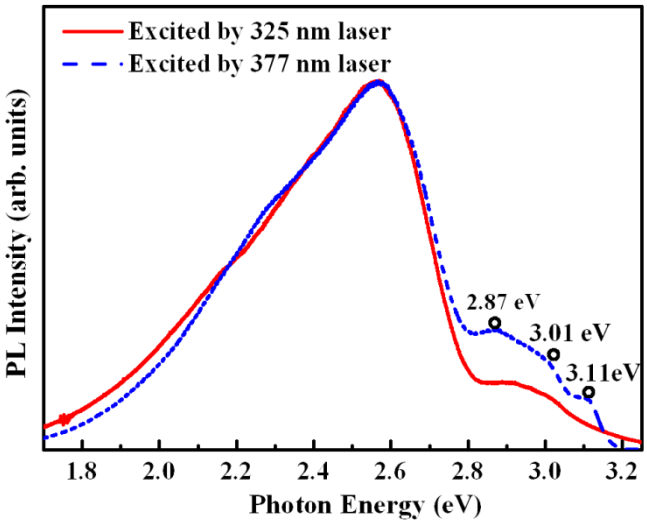

(d)

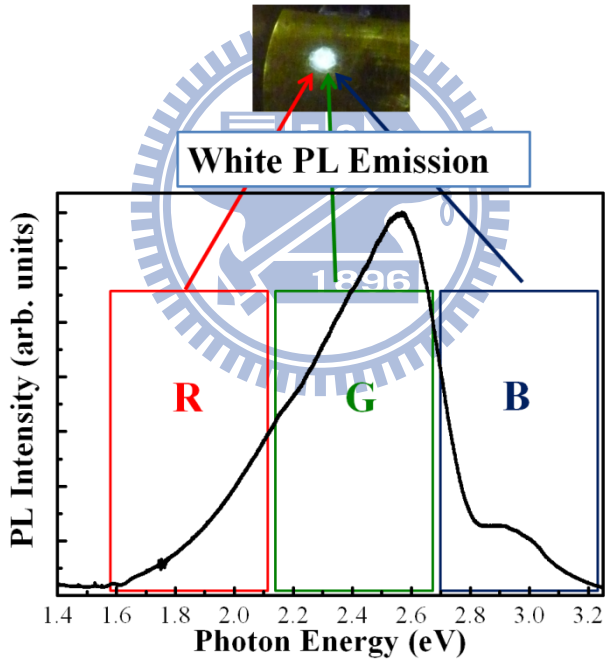

Fig. 3 (a) PL spectra of the graded $Zn_{1-x}Cd_xO$ and the $Zn_{0.741}Cd_{0.259}O$ at 10 K. The inset shows the PL spectra with log scale. **(b)** Transmittance spectra of the graded $Zn_{1-x}Cd_xO$ and the $Zn_{0.741}Cd_{0.259}O$ at 10 K. **(c)** PL spectra obtained at 10 K from the graded $Zn_{1-x}Cd_xO$ using different excitation (325 nm and 377 nm). **(d)** White PL emission can be observed by naked eye.

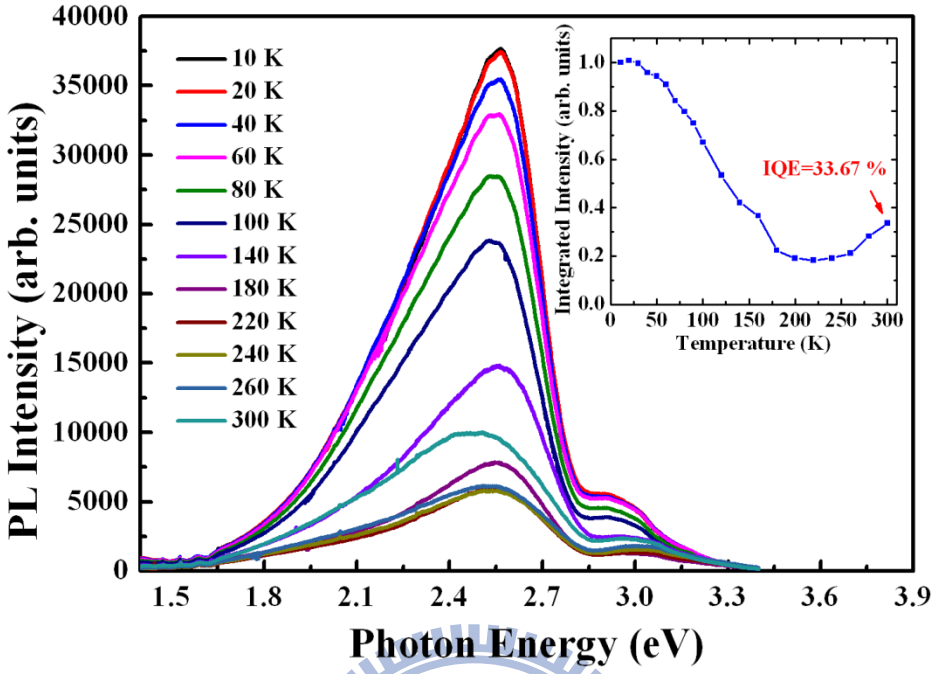

Fig. 4 PL spectra of the graded $Zn_{1-x}Cd_xO$ film at various temperatures. The inset shows integrated PL intensities as a function of temperature for the graded $Zn_{1-x}Cd_xO$ film.

(a)

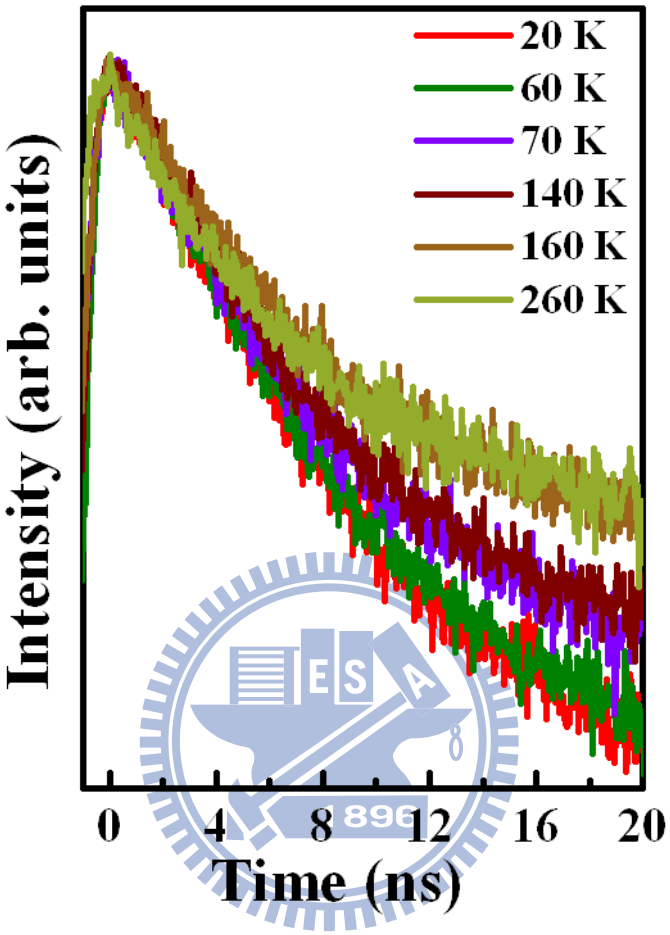
20 K
60 K
70 K
140 K
160 K
260 K
Intensity (arb. units)
0
4
8
12
16
20
Time (ns)

(b)

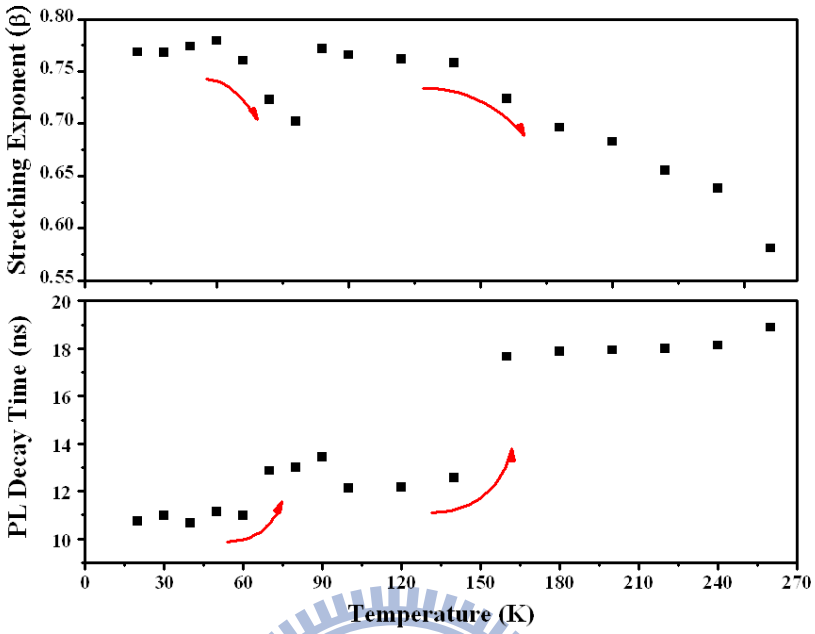
Stretching Exponent (β)
0.80
0.75
0.70
0.65
0.60
0.55
PL Decay Time (ns)
20
18
16
14
12
10
0
30
60
90
120
150
180
210
240
270
Temperature (K)

(c)

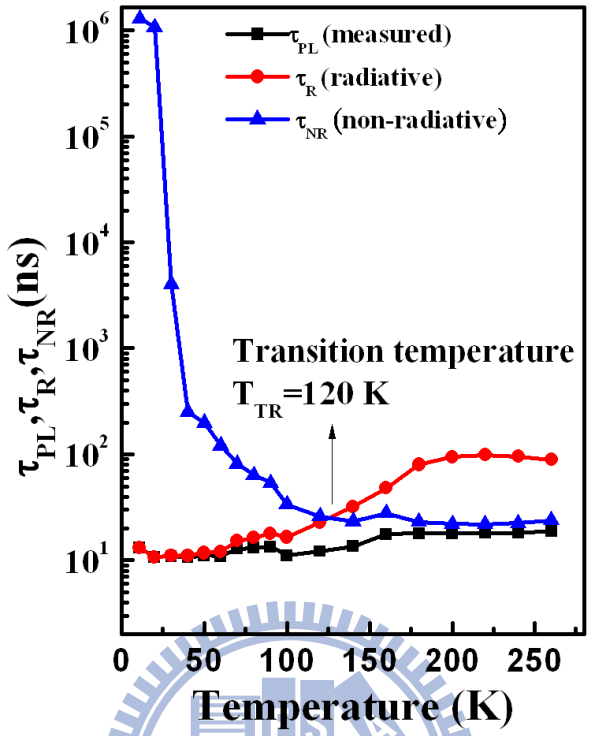

Fig. 5 (a) PL intensity decay as a function of temperature. **(b)** PL decay time and stretching exponent (β) of graded $Zn_{1-x}Cd_xO$ as a functions of temperature. **(c)** Temperature dependence of measured PL decay time along with the extracted radiative and nonradiative lifetime parameters. The transition temperature T_{TR} is indicated by an arrow.

References

[1] A. Tsukazaki, A. Ohtomo, T. Onuma, M. Ohtani, T. Makino, M. Sumiya, K. Ohtani, S. F. Chichibu, S. Fuke, Y. Segawa, H. Ohno, H. Koinuma, M. Kawasaki, Nature Mater. **4**, 42 (2005).

[2] E. Ohshima, H. Ogino, I. Niikura, K. Maeda, M. Sato, M. Ito, and T. Fukuda, J. Cryst. Growth **260**, 166 (2004).

[3] J. M. Ntep, S. S. Hassani, A. Lusson, A. Tromson-Carli, D. Ballutaud, G. Didier, and R. Triboulet, J. Cryst. Growth **207**, 30 (1999).

[4] D. C. Look, Mater. Sci. Eng., B **80**, 381 (2001).

[5] D. M. Bagnall, Y. F. Chen, Z. Zhu, T. Yao, S. Koyama, M. Y. Shen, and T. Goto, Appl. Phys. Lett. **70**, 2230 (1997).

[6] J. H. Lim, C. K. Kong, K. K. Kim, I. K. Park, D. K. Hwang, and S. J. Park, Adv. Mater. **18**, 2720 (2006).

[7] S. Lizng, H. Sheng, Y. Liu, Z. Huo, Y. Lu, and H. Shen, J. Cryst. Growth **225**, 110 (2001).

[8] M. Law, L. E. Greene, J. C. Johnson, R. Saykally, and P. Yang, Nat. Mater. **4**, 455 (2005).

[9] Q. Wan, Q. H. Li, Y. J. Chen, T. H. Wang, X. L. He, J. P. Li, and C. L. Lin, Appl. Phys. Lett. **84**, 3654 (2004).

[10] Y. Chen, D. M. Bagnall, H. J. Koh, K. T. Park, K. Hiraga, Z. Q. Zhu, and T. Yao, J. Appl. Phys. **84**, 3912 (1998).

[11] Y. F. Chen, H. J. Ko, S. K. Hong, T. Yao, Appl. Phys. Lett., **76**, 559 (2000).

[12] R. D. Shannon, Acta Crystallogr., Sect. A: Cryst. Phys., Diffr., Theor. Gen. Crystallogr. **32**, 751 (1976).

[13] J. K. Furdyna, J. Appl. Phys. **64**, R29 (1988).

[14] T. Dietl, H. Ohno, F. Matsukara, J. Gilbert, and D. Ferrand, *Science* **287**, 1019 (2000).

[15] F. P. Koffyberg , Phys. Rev. B **13**, 4470 (1976).

[16] W. F. Yang, R. Chen, B. Liu, G. G. Gurzadyan, L. M. Wong, S. J. Wang, and H. D. Sun, Appl. Phys. Lett. **97**, 061104 (2010).

[17] Th. Gruber, C. Kirchner, R. Kling, F. Reuss, A. Waag, F. Bertram, D. Forster, J. Christen, and M. Schreck, Appl. Phys. Lett. **83**, 3290 (2003).

[18] J. Ishihara, A. Nakamura, S. Shigemori, T. Aoki, and J. Temmyo, Appl. Phys. Lett. **89**, 091914 (2006).

[19] S. Sadofev, S. Blumstengel, J. Cui, J. Puls, S. Rogaschewski, P. Schäfer, and F. Henneberger, Appl. Phys. Lett. **89**, 201907 (2006).

[20] H. J. Ko, T. Yao, Y. Chen, and S. K. Hong, J. Appl. Phys. 92, 4354 (2002).

[21] Y. Chen, D. M. Bagnall, H.J. Koh, K.T. Park, K. Hiraga, Z. Zhu, and T. Yao, J.

Appl. Phys. **84**, 3912 (1998).

[22] X. L. Wu, G. G. Siu, C. L. Fu, H. C. Ong, Appl. Phys. Lett. **78**, 2285 (2001).

[23] S. Sadofev, S. Blumstengel, J. Cui, J. Puls, S. Rogaschewski, P. Schäfer, Yu, G. Sadofyev, and F. Hennebergerb, Appl. Phys. Lett. **87**, 091903 (2005).

[24] Hong Seong Kang, Jae Won Kim, Jong Hoon Kim, Sang Yeol Lee, Y. Li, Jang-Sik Lee, J. K. Lee, M. A. Nastasi, S. A. Crooker, and Q. X. Jia, J. Appl. Phys. **99**, 066113 (2006).

[25] T. Fukumura, Zhengwu Jin, A. Ohtomo, H. Koinuma, and M. Kawasaki, Appl. Phys. Lett. **75**, 3366 (1999).

[26] K. Samanta, S. Dussan, R. S. Katiyar, and P. Bhattacharya, Appl. Phys. Lett. **90**, 261903 (2007).

[27] C. A. Johnson, K. R. Kittilstved, T. C. Kaspar, T. C. Droubay, S. A. Chambers, G. M. Salley, and D. R. Gamelin, Phys. Rev. *B* **82**, 115202 (2010).

[28] T. Mizokawa, T. Nambu, A. Fujimori, T. Fukumura, and M. Kawasaki, Phys. Rev. B **65**, 085209 (2002).

[29] R. Cusco, E. Alarcon-Llado, J. Ibanez, L. Artus, J. Jimenez, B. Wang, and M. J. Callahan, Phys. Rev. B **75**, 165202 (2007).

[30] K. W. Boer, *Survey of Semiconductor Physics: Electrons and Other Particles in Bulk Semiconductors* (1990).

[31] J. F. Scott, T. C. Damen, W. T. Silfvast, R. C. C. Leite, and L. E. Cheesman, Optics Commun. **1**, 397 (1970).

[32] M. C. Klein, F. Hache, D. Ricard, and C. Flytzanis, Phys. Rev. B **42**, 11123 (1990).

[33] P. Lautenschlager, M. Garriga, and M. Cardona, Phys. Rev. B **36**, 4813 (1987).

[34] R. M. Martin and C. M. Varma, Phys. Rev. Lett. **26**, 1241 (1971).

[35] W. H. Sun, S. J. Chua, L. S. Wang, and X. H. Zhang, J. Appl. Phys. **91**, 4917 (2002).

[36] A. Teke, U. Ozgur, S. Dogan, X. Gu, H. Morkoc, B. Nemeth, J. Nause, H.O. Everitt, Phys. Rev. B: Condensed Matter **70**, 195207 (2004).

[37] J. F. Muth, R. M. Kolbas, A. K. Sharma, S. Oktyabrsky, Narayan, J. Appl. Phys. **85**, 7884 (1999).

[38] Th. Gruber, C. Kirchner, R. Kling, F. Reuss, A. Waag, F. Bertram, D. Forster, J. Christen, M. Schreck, Appl. Phys. Lett. **83**, 3290 (2003).

[39] Hong Seong Kang, Sung Hoon Lim, Jae Won Kim, Hyun Woo Chang, Gun Hee Kim, Jong-Hoon Kim, Sang Yeol Lee, Y. Li, Jang-Sik Lee, J. K. Lee, M. A. Nastasi, S. A. Crooker, Q. X. Jia, J. Cryst. Growth **287**, 70–73 (2002).

[40] C. S. Yang, D. Y. Hong, C. Y. Lin, W. C. Chou, C. S. Ro, W. Y. Uen, W. H. Lan, S. L. Tu, J. Appl. Phys. **83,** 2555 (1998).

[41] Juri Krustok, Heikki Collan, Kari Hjelt, J. Appl. Phys. **81**, 1442 (1997).

[42] Y. P. Varshni, Physica, **34**, 149 (1967).

[43] Y. Z. Zhu, G. D. Chen, Honggang Ye, Aron, Walsh, C. Y. Moon, and Su-Huai Wei, Phys. Rev B, **77**, 245209 (2008).

[44] J. Ishihara, A. Nakamura, S. Shigemori, T. Aoki, and J. Temmyo, Appl. Phys. Lett. **89**, 091914 (2006).

[45] Hong Seong Kang, Jae Won Kim, Jong Hoon Kim, Sang Yeol Lee, Y. Li, Jang-Sik Lee, J. K. Lee, M. A. Nastasi, S. A. Crooker, and Q. X. Jia, J. Appl. Phys. **99**, 066113 (1998).

[46] Yan-Cheng Lin, Wei-Shi Jiang, Wu-Ching Chou, Wei-Kuo Chen, Wen-Hao Chang, Chin-Hau Chia, Cheng-Yu Chen, and Jen-Inn Chyi, Appl. Phys. Lett. **100**, 071912 (2012).

[47] F. Bertam, S. Giemsch, D. Forster, J. Christen, R. Kling, C. Kirchner, A. Waag, Direct imaging of phase separation in ZnCdO layers, Appl. Phys. Lett. **88**, 061915 (2006).

[48] G. Saint-Girons and I. Sagnes, J. Appl. Phys. **91**, 10115 (2002).

[49] S. Watanabe, N. Yamada, M. Nagashima, Y. Ueki, C. Sasaki, Y. Yamada, T. Taguchi, K. Tadatomo, H. Okagawa, and H. Kudo, Appl. Phys. Lett. **83**, 4906 (2003).

[50] A. Sasaki, S. Shibakawa, Y. Kawakami, K. Nishizuka, Y. Narukawa, and T. Mukai, Jpn. J. Appl. Phys. **45**, 8719 (2006).

[51] Mareike Trunk, Vishnukanthan Venkatachalapathy, Tianchong Zhang, Alexander Azarov, Augustinas Galeckas, and Andrej Yu. Kuznetsov, Phys. Status Solidi C, **9**, 1805 (2012).

[52] Shao-Ying Ting, Yu-Feng Yao, Wei-Lun Chung, Wen-Ming Chang, Chih-Yen Chen, Hao-Tsung Chen, Che-Hao Liao, Horng-Shyang Chen, Chieh Hsieh, and C. C. Yang, OPTICS EXPRESS, **20**, 21860 (2012).

[53] J. C. Phillips, Rep. Prog. Phys. **59**, 1133 (1996).

[54] M. Gurioli, A. Vinattieri, M. Colocci, C. Deparis, J. Massies, G. Neu, A. Bosacchi, and S. Franchi, Phys. Rev. B **44**, 3115 (1991).

[55] M. Kubota, T. Onuma, A. Tsukazaki, A. Ohtomo, M. Kawasaki, T. Sota, and S. F. Chichibu, Appl. Phys. Lett. **90**, 141903 (2007).

[56] S. F. Chichibu, T. Onuma, M. Kubota, A. Uedono, T. Sota, A. Tsukazaki, A. Ohtomo, and M. Kawasaki, J. Appl. Phys. **99**, 093505 (2006).

Chapter 8

Conclusion

In this dissertation, high quality of ZnO, $Zn_{1-x}Mg_xO$, $Zn_{1-x}Mn_xO$ and $Zn_{1-x}Cd_xO$ thin films were grown on c-Al_2O_3 using the SVT Associates PA-MBE system. Additionally, the optical properties of these alloys were also investigated. The growth parameters of high quality ZnO thin films were used for the growth of $Zn_{1-x}Mg_xO$, $Zn_{1-x}Mn_xO$ and $Zn_{1-x}Cd_xO$ epilayers. For the $Zn_{1-x}Mg_xO$ thin films, the MgO buffer is very effective on the improvement of surface morphology during the initial growth stage, which eventually leads to an atomically flat surface. The maximum emission energy of 3.71 eV for the $Zn_{0.888}Mg_{0.112}O$ sample was observed. The energy of strong absorption edge increases with the Mg concentration. Additionally, ZnO/ZnMgO multiple QWs were also fabricated successfully.

In the case of $Zn_{1-x}Mn_xO$ thin films, we have grown $Zn_{1-x}Mn_xO$ (x=0-0.061) thin films by MBE. From RRS spectra, we observe LO phonon lines up to 5 and 11 order for ZnO and ZnMnO samples, respectively. From the temperature dependent RRS experiment, we find the intensities of these LO phonon lines are sensitive to the band gap position. Low temperature PL spectra of $Zn_{0.997}Mn_{0.003}O$ at magnetic field B=0 T and 5 T were investigated to calculate the degrees of circular polarization of P=0%

and 9%, respectively.

In the case of $Zn_{1-x}Cd_xO$ thin films, the growth and carrier dynamics of $Zn_{1-x}Cd_xO$ were investigated. High quality $Zn_{1-x}Cd_xO$ thin films with visible light emission were grown on sapphire substrates by PA-MBE. The maximum concentration of Cd is 49.7 %, which can be systematically adjusted via the Cd/Zn beam pressure ratio. The S-shaped dependence of the PL peak positions indicates that Cd_n bound exciton dominates the other localized states. The V-shaped dependence of the PL peak energy in high Cd concentration $Zn_{1-x}Cd_xO$ indicates that Cd_n clusters bound exciton, in which the carriers are deeply trapped below 150 K, is the major origin of emission. Above 150 K, the carriers can escape from the deepest localized Cd_n clusters states to shallow localized Cd_n states. An activation energy E*a*=15 meV was observed in $Zn_{0.634}Cd_{0.366}O$, and the corresponding thermal energy around 150 K, coincides the temperature where the blue shift starts and integrated PL intensity increases.

Finally, the white PL emission of the graded $Zn_{1-x}Cd_xO$ film was fabricated. The origin of radiative recombination and dynamics of the charge carriers in the graded $Zn_{1-x}Cd_xO$ multilayers is investigated by PL and TRPL spectroscopy. We confirmed that the broad band emission is due to the NBE emission and localized states emission of $Zn_{1-x}Cd_xO$. The IQE of our sample reaches 33.67 %. Strong evidence of exciton

transfer from the deep localized state to the shallow localized state was observed. In addition, the radiative and non-radiative recombination arrive balance at high temperature. This result corroborates with the phenomena that the PL intensity increases at high temperature. The high IQE of $Zn_{1-x}Cd_xO$ proposes this material has potential application in high efficiency photonic devices.

Publications

1. **K. F. Chien** , W. L. Hsu , A. J. Tzou , Y. C. Lin , W. C. Chou, L. Lee , C. H. Chia , C. S. Yang, "Thermal-activated carrier transfer in ZnCdO thin film grown by plasma-assisted molecular beam epitaxy", Journal of Crystal Growth, 378, 208-211 (2013).

2. **K. F. Chien**, Y. L. Yang , A. J. Tzou , W. C. Chou, "Optical properties of $Zn_{1-x}Mn_xO$ thin films grown by molecular beam epitaxy", Journal of Crystal Growth, 378, 218-221 (2013).

3. A. J. Tzou a, **K. F. Chien**, H. Y. Lai, J. T. Ku, L. Lee, W. C. Fan, W. C. Chou, "The study of self-assembled ZnO nanorods grown on Si(111) by plasma-assisted molecular beam epitaxy", Journal of Crystal Growth, 378, 466-469 (2013).

4. Ling Lee, Wen-Chung Fan, **Kun-Feng Chien**, An-Jye Tzou , Wu-Ching Chou, "Growth evolution and magneto-optical characteristics of self-assembled ZnTe/ZnMnSe quantum dots", Journal of Crystal Growth, 378, 222-225 (2013).

5. Ling Lee, **Kun-Feng Chien**, Wu-Ching Chou, Chih-Hsin Ko, Cheng-Hsien Wu, You-Ru Lin, Cheng-Tien Wan, Clement H. Wann, Chao-Wei Hsu, Yung-Feng Chen and Yan-Kuin Su, "Improvement of defect reduction in semi-polar GaN grown on shallow-trenched Si(001) substrate", CrystEngComm, 14, 4486–4489 (2012).

6. **Ling Lee, Kun-Feng Chien, Wen-Chung Fan, Wu-Ching Chou, Chih-Hsin Ko, Cheng-Hsien Wu1, You-Ru Lin, Cheng-Tien Wan, Clement H. Wann, Chao-Wei Hsu, Yung-Feng Chen, and Yan-Kuin Su, "Optical Studies of GaAs Nanowires Grown on Trenched Si(001) Substrate by Cathodoluminescence" Japanese Journal of Applied Physics 51 (2012).**

7. **C. S. Yang, K. F. Chien, J. Y. Lai, C. W. Luo, W. C. Chou, Y. T. Shih, J. S. Wang, S. R. Jian, "Carrier Dynamics in Self-Assembled CdTe Stranski-Krastanow Quantum Dots Grown on ZnSe by Molecular Beam Epitaxy", Journal of the Korean Physical Society, 53, 5, (2008).**